POLITECNICO
MILANO 1863

SCUOLA DI INGEGNERIA INDUSTRIALE
E DELL'INFORMAZIONE

X-ray Raman characterization of CO to CO_2 Conversion on Au/CeO_2 Substrate

Tesi di Laurea Magistrale in
Engineering Physics

Author: **Eugenio Bianchi**

Student ID: 945545
Advisor: Prof. Marco Moretti
Co-advisors: Alessandro Longo, Christoph J. Sahle
Academic Year: 2022-23

Abstract

Technologies for the conversion and removal of hazardous gasses are becoming indispensable to the fight on man made climate change. Ceria with gold nanoparticles precipitated on the its surface has shown interesting properties for this topic, catalysing the conversion CO to CO_2, thanks to its oxygen storage capacity (OSC), it allows for the removal of this toxic species from the combustion exhaust gasses in the industry and automotive sector. The easy uptake and release of O from its lattice it is bonded to change of the oxidation state (OS) of some of its cerium ions. In the interchange between the Ce^{3+} and Ce^{4+} OS, Ce $4f$ electron play a key role. The scope of this thesis is following the change in the OS of Ce ions, connected to the release/uptake of oxygen by the substrate, through the changes in the the spectral features of the Ce $N_{4,5}$ excitation edge, involving Ce $4d$ and $4f$ levels. This analysis led to the quantification of the ratio between Ce^{4+}/Ce^{3+}. *In situ* X-ray Raman Scattering (XRS) spectroscopy experiments, sensitive to the electronic configuration of the sample under study, have been conducted at the ID20 beamline at ESRF. The $N_{4,5}$ excitation edge has been scanned and the edge and pre-edge feature measured. To build a reference for the experiments, multiplet calculations have been performed with the Hilbert++ code to simulate the spectral features of the $N_{4,5}$ edge for Ce^{4+}, with electronic structure [Xe]$4d^0$, and Ce^{3+}, [Xe]$4d^1$. The hybridization of the Ce^{4+} $5d$ and $4f$ states, with the O $2p$ states is discussed to explain the spectral features. Upon CO and temperature treatment, a conversion from Ce^{4+} to Ce^{3+} for roughly 30% of the original Ce has been observed.

Keywords: XRS, Ceria, Catalysis, Climate change, Gold nanoparticles

Abstract in Italiano

Tecnologie per la conversione e la rimozione di gas pericolosi stanno diventando indispensabili per combattere il cambiamento climatico causato dall'uomo. Ceria con nanoparticelle d'oro precipitate sulla sua superfice ha mostrato delle proprietà interessanti per questo argomento, catalizando la conversione di CO a CO_2, grazie alla sua capacità di imagazzinare e rilasciare ossigeno, permette di rimuovere questa specie dal gas esausto di combustione emesso dalle industrie e dal settore dei transporti. Il facile assorbimendo e rilascio di O dalla sua struttura cristallina è legato al cambio dello stato di ossidazione (OS) di alcuni dei suoi ioni di cerio. Nel cambio tra lo OS Ce^{3+} e Ce^{4+}, gli eletroni $4f$ giocano un ruolo chiave. Lo scopo di questa tesi è seguire il cambio di OS negli ioni di Ce, connesso all'assorbimento e al rilascio di O dal substrato, attraverso i cambiamenti nello spettro della $N_{4,5}$ excitation edge del Ce, avente a che fare con gli elettroni del Ce negli stati $4d$ e $4f$. Questa analisi ha condotto alla quantificazione del rapporto tra Ce^{4+}/Ce^{3+}. Degli esperimenti *In situ* di spettroscopia Raman a X-ray (XRS), sensibile alla configurazione elettronica del campione sotto studio, sono stati condotti alla beamline ID20 dell'ESRF. L'excitation edge $N_{4,5}$ è stata scansionata e le proprietà dell'edge e del pre-edge sono state misurate. Per costruire dei riscontri teorici per l'esperimento, delle simulationi dell'edge $N_{4,5}$ sono state effettuate mediante calcoli di multipletti con il codice Hilbert++, per il Ce^{4+}, con la struttura elettronica [Xe]$4d^0$, e per il Ce^{3+}, con la struttura [Xe]$4d^1$. L'ibridizzazione degli stati $5d$ e $4f$ del Ce^{4+}, con quelli $2p$ dell'O è stata discussa per spiegare le proprietà dello spettro. Di seguito al trattamento CO, una converisione di Ce^{4+} a Ce^{3+} è stata osservata, fino ad arrvare al 30% del totale di Ce.

Keywords in Italiano: XRS, Ceria, Catalissi, Cambiamento Climatico, Nanoparticelle d'Oro

Contents

Abstract **i**

Abstract in Italiano **iii**

Contents **v**

1 Introduction
Why do we play? **1**
1.1 Motivation 1
1.2 Au/CeO_2, metal metal-oxide interaction 2
1.3 Ceria reduction/oxidation 5
1.4 Goals 8
1.5 Reflection on REE and the environment 9

2 Multiplets and Matrix Elements
The rules of the game **11**
2.1 Multiplet theory 11
2.1.1 Atomic Hamiltonian for an isolated ion 11
2.1.2 Crystal field effects 13
2.2 X-ray Raman scattering 14
2.2.1 Matrix element 15
2.2.2 $|\,f\,\rangle$ and $|\,i\,\rangle$ for Ce 18

3 Experimental techniques and setup
Toys, tactics and playing field **21**
3.1 ESRF 21
3.2 ID20 21
3.3 Large-solid-angle XRS spectrometer 22
3.4 Experiment and sample preparation 24

3.4.1 Sample . . . 24
3.4.2 Experiment . . . 25

4 Data analysis
VAR **29**
4.1 XRStools . . . 29
4.2 Experimental data . . . 32

5 Results
Scoreboard **35**
5.1 Hilbert++ . . . 35
5.2 Location . . . 38
5.3 Quantification . . . 42

6 Conclusion
After match **45**
6.1 The $N_{4,5}$ edges and pre-edges . . . 45
6.2 Gold Role . . . 45
6.3 Hybridization effects . . . 46
6.4 How to improve the research . . . 46

Bibliography **49**

List of Figures **57**

A Appendix A
code example **59**
A.1 h++ . . . 59
A.2 Python scripts . . . 65

B Appendix B
Synchrotron beam properties **71**
B.1 Relativistic effects . . . 71
B.2 Undulators . . . 74

Acknowledgements **77**

1 | Introduction

Why do we play?

1.1. Motivation

The rapid climate change has lately focused a lot of attention on new mitigation and adaptation techniques to reduce and coexist with the damages caused by the current society fossil-fuels-based for energy production. Carbon capture, hazardous gasses conversion and removal, hydrogen production for fuel cell and other technologies are about to become indispensable to achieve the UN's Sustainable Development Goals (SDGs).

Since the 1970s, a great deal of research has been conducted on reducible rare earth element (REE) substrates even though it is only relatively lately that the research done on these materials has increased greatly, thanks to their relative easier access. REE based materials act as optimum catalysts and catalysts support [1], their application ranges from the long known three way catalyst (TWC) for CO conversion [2–4], inverse catalysts [5, 6] for the CO_2 conversion, as well as active photocatalysts [7], to the application in solid oxide fuel cells (SOFCs) [8] and the water-gas shift (WGS) reaction for the production of hydrogen [9–14]. Thorough reviews on the physics and applications of these materials can be easily found online [15–20] and are recommended for anyone who is interested in deepening their knowledge on the subject.

Because of its unique high oxygen storage capacity (OSC), cerium(IV) oxide, CeO_2 or ceria, remains one of the main REE oxides studied for catalytic purposes. Much research, both experimental and computational, has been conducted and a large number of papers have been published on this topic. The OSC of ceria is given by its redox properties; switching between the Ce^{4+} and the Ce^{3+} oxidation state of cerium, two Ce ions can accommodate the two extra electrons left behind by the release of an oxygen at the surface, $O^{2-} + 2Ce^{4+} = 1/2\ O(g) + 2Ce^{3+}$, leaving an O vacancy on the lattice surface. The vacancies can later be accommodated into the sublattice. The formation of vacancies on the surface is correlated then to the release of oxygen, which is now strongly believed to

be the direct *responsible* for the CO oxidation; following the equation $O_s + CO_{ads} = V_O^{++} + 2e^- + (1/2\ O(g) + CO) = V_O^{++} + 2e^- + CO_2$ [1]. An oxygen from the surface oxidizes an adsorbed CO molecule, in this process an oxygen vacancy is left behind on the surface with two extra electrons, while the CO_2 molecule is released. The two extra electrons reduce two Ce ions in the lattice, namely the next nearest and nearest neighbours to the vacancy [21–23]. The local structure of Ce ions is shown in Figure 1.1.

The formation and the thermalization of oxygen vacancies is an interesting topic widely studied in literature, the localization and cluster formation on the surface [4, 24, 25], in the subsurface [26] or in the bulk [7, 19] has been investigated. The behavior of such vacancy is crucial for the catalytic activity of ceria and ceria-based material. These vacancies are often the active site the catalytic activity [12, 27], as well as anchor point for other particles[2], whose interaction strongly enhance the activity [2, 4, 9, 28].

1.2. Au/CeO_2, metal metal-oxide interaction

The activity of gold for CO conversion has been long long studied [1, 2, 29], Au on a ceria substrate facilitates the vacancy formation process and lowering the reaction temperature, enhances the catalytic activity and the CO conversion to CO_2. Already in a paper published in 1987 by Masatake Haruta et al. the improvements due to the addition of Au were pointed out. CO conversion could happen at temperatures close to -70 °C and on metal oxides as Fe_2O_3, Co_3O_4 or NiO when they were coupled with this noble metal [2].

Ceria is a reducible metal oxide, it can easily accept electrons from a donor species, like a metal; the excess electrons thermalize on the d and f levels of the metal cation of the oxide. The deposition of Au nanoparticles (NPs) on ceria surface transfers some valence electrons of the noble metal to the $4d$ orbitals of some of the Ce ions, reducing them from Ce^{4+} to Ce^{3+} [30] [3].

The contact between the metal and the oxide produces a Schottky junction, some electrons flow from the metal to the oxide creating a negatively charge region on the oxide close to the interface and a positively charged one in the metal. This is correlated with the formation of a small potential that can change the electronic structure of the oxide and create new active site for catalysis. [31] In ceria, the release of oxygen ion leaves behind

[1] Following recent studies, when Au nanoparticles are involved, it might be a Au-CO species that participate to this reaction, see later.

[2] These particle can range from single ionic species to NPs, as well as the inverse, NPs of ceria on other substrates [8]

[3] On stoichiometric ceria, the adsorption of Au does not promotes the formation of vacancy, while on (110) and (100) ceria it does

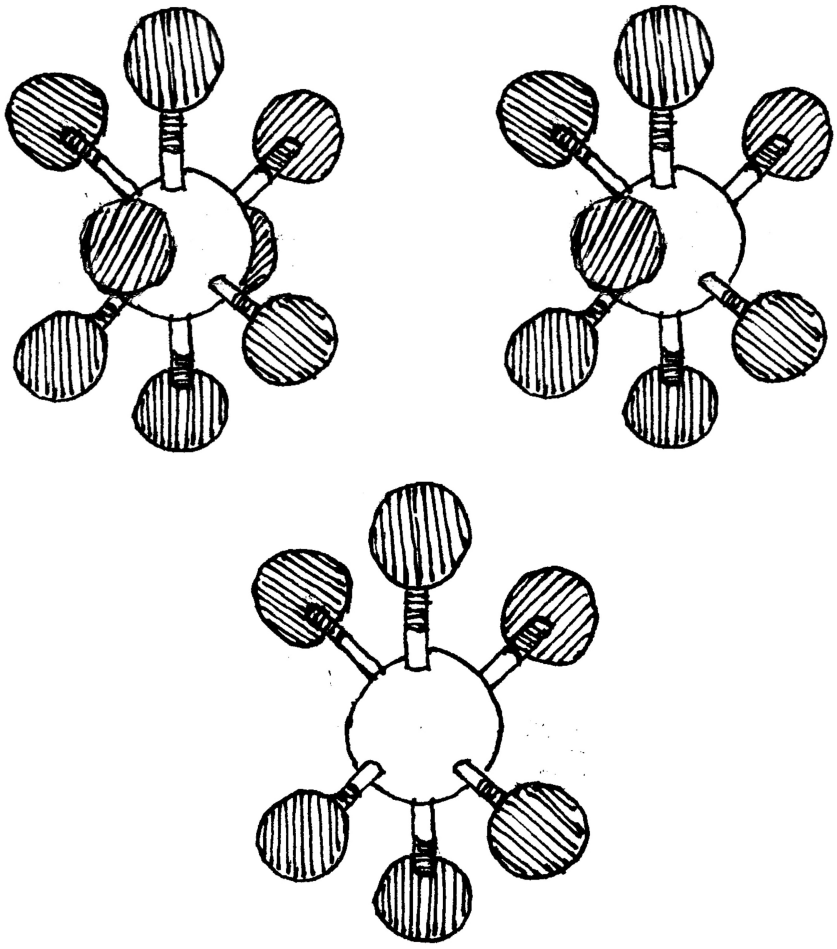

Figure 1.1: On the top left: schematic structure of an 8-fold coordinated Ce ion with shown the oxygen bounds, the white center sphere is the Ce ion and the black ones are the oxygen ions. On the top right the same schematics for a 7-fold coordinated Ce ion. On the bottom is shown a 6-fold coordinated Ce ion. The 8-fold coordinated Ce ion is not coordinated to any vacancy; in an ideal completely oxidized ceria, all Ce ions have this local structure and are all Ce^{4+} species. In an ideal completely reduced ceria, c-Ce_2O_3, all Ce ions have the 6-fold local structure and are Ce^{3+}. For this reason the study conducted by [21–23] are important to show that in partially reduced ceria the bigger Ce^{3+} species prefer localize in the 8 and eventually 7-fold coordinated local structure.

an O vacancy and two electrons, that proceed to reduce two Ce^{4+} to Ce^{3+} localizing as a single electron on the $4f$ orbital, and shifting the core levels binding energies. In defective ceria, the deposition of Au NPs is linked to a charge transfer from the support to the metal, the single electron on the $4f$ orbital of Ce is transferred to the the $6s$ orbital of Au to form a pair with the other electron already present there, with the consequence of obtaining a negatively charged supported metal. The valence of the supported metal is therefore dependent on the local presence of oxygen vacancy. In both cases, the exchange of charges stabilizes the Au adsorption [32].

Au on reducible oxides also promotes the adsorption on its surface of CO molecules. In [33] is studied the O2 activation by Au, Au catalysis also consists in the adsorption of O2 on its surface and the activation of this molecular species for the CO conversion, this is possible only at low temperatures (77 k) as then the oxygen becomes unstable and desorbs from the Au NPs (at 170 k).It is shown that one of the role of Au is that of facilitating the adsorption of CO molecules on its surface at higher temperature and at lower partial pressures with respect to the one that are necessary for bare metal oxides, ceria in our case. The higher temperature pathway proposed and studied were four, three of which involve the molecular oxygen adsorbed either on the Au NPs surface, at its interface with the reducible metal or at the interface at an O vacancy of the oxide; and one that involves the release of an O from the substrate lattice and the generation of an O vacancy at the interface. In the latter case, molecular oxygen would simply re-oxidize the substrate once the CO conversion has taken place. The evidence that the catalytic activity and the OSC increase linearly with the length of the peripheral sites of the Au NP strongly suggested that the active sites were at the interface Au/CeO_2. The support effect on the Au catalytic activity is demonstrated and known, either directly participating as in this case or indirectly by shaping the Au NPs. It is shown how reducible oxides produce active catalysts support whereas non-reducible oxides produce inactive catalysts support.

The direct evidence of the participation of the oxygen vacancy to the CO conversion on the peripheral area of the Au NPs has been shown by [34].

Recent studies balanced the performance of different Au/CeO_2 interfaces, taking into consideration morphologies, concentration, particle size [35, 36], temperature, species [10], etc..; comparing Au single ionic species to disordered clusters (< 2 nm) and Au NPs (3, 4 nm) [12]. Nevertheless Au NPs have shown promising activation properties for the conversion of CO to CO_2. D. Widmann and R. J. Behm studied the mechanism of the reaction. Out of the four mechanism proposed, they found out that the main dynamic of this reaction is a Mars-van Krevelen mechanism [33]. At the peripheral area of the Au NP, a CO particle adsorbed to the gold reacts with an oxygen from the sublattice and converts to CO_2 leaving a negatively charged oxygen vacancy on the partially reduced support.

The two electrons left behind proceed reducing Ce^{4+} ions to Ce^{3+} [4, 20]. Further studies on the modification of the electronic configuration and its evolution during the reaction are still needed since they could be used to study the oxygen vacancy formation.

1.3. Ceria reduction/oxidation

The process of oxidation of ceria has been for long under investigation and subject of controversy among the scientific community [20]. The role of gold and other noble metal NPs has been studied, and among the various surface mechanisms that were proposed to explain the behavior, from [33] the following scheme emerges. The CO molecules are adsorbed on the surface of the Au NPs. The adsorbed CO molecules move on the surface of the Au NPs and can *spill over* the Au/CeO_2 interface. At the interface an oxygen atom is removed by the CO and CO_2 is formed, leaving an oxygen vacancy behind, as depicted in Figure 1.2.

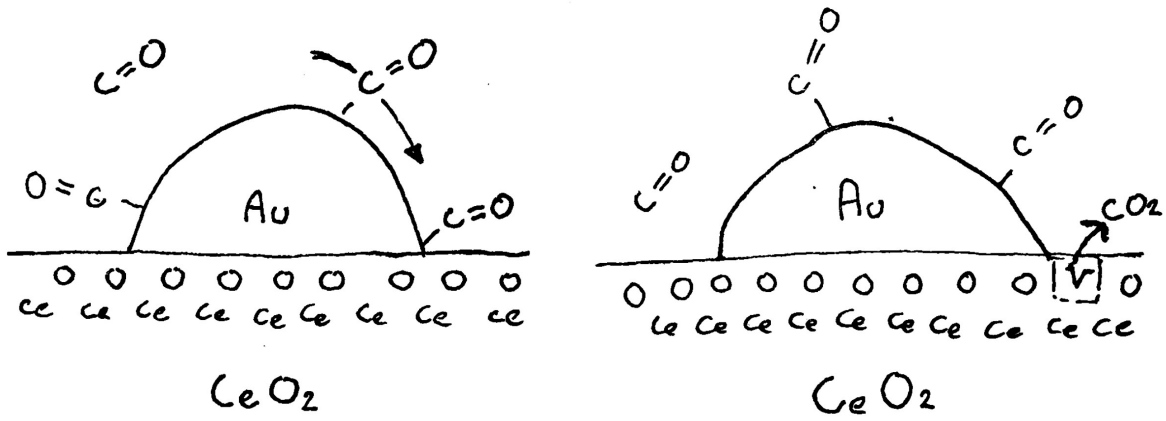

Figure 1.2: Dynamics of the spill over redox process. Some CO molecules are adsorbed by the Au NP and they can spill over on the ceria substrate. There the oxygen ions can activate and oxidize the CO molecule and convert it into a CO_2 molecule, leaving an oxygen vacancy behind.

In aerobic condition, some molecular oxygen would split at the oxygen vacancy in the oxide and fill it. If this does not happen fast enough, the oxygen vacancy can move and accumulate inside the ceria substrate in the subsurface or in the bulk. This *spill over* model is also confirmed by other studies that took into consideration also the role of particle size. What emerges from DFT dynamic simulation and TEM observation is that relative large Au NPs (> 4 nm) remain unmoved after the sample exposure to CO containing environment, whereas smaller NPs (>2 nm) present strong dynamic behavior

[37], dynamic low coordinated Au atoms are generated, and they strongly contribute to the catalysis enhancing the performances for CO conversion. Other studies suggest that CO, once adsorbed, it bounds with a Au atom and form a separated species. It is this species that moves over the surface of the NP to the Au/ceria interface [38]. It also emerges that the Au atom bounded to the CO may leave briefly the Au NP, and once the CO molecule oxidises, it is reintegrate in the NP [39]. The schematics of this process is shown in Figure 1.3.

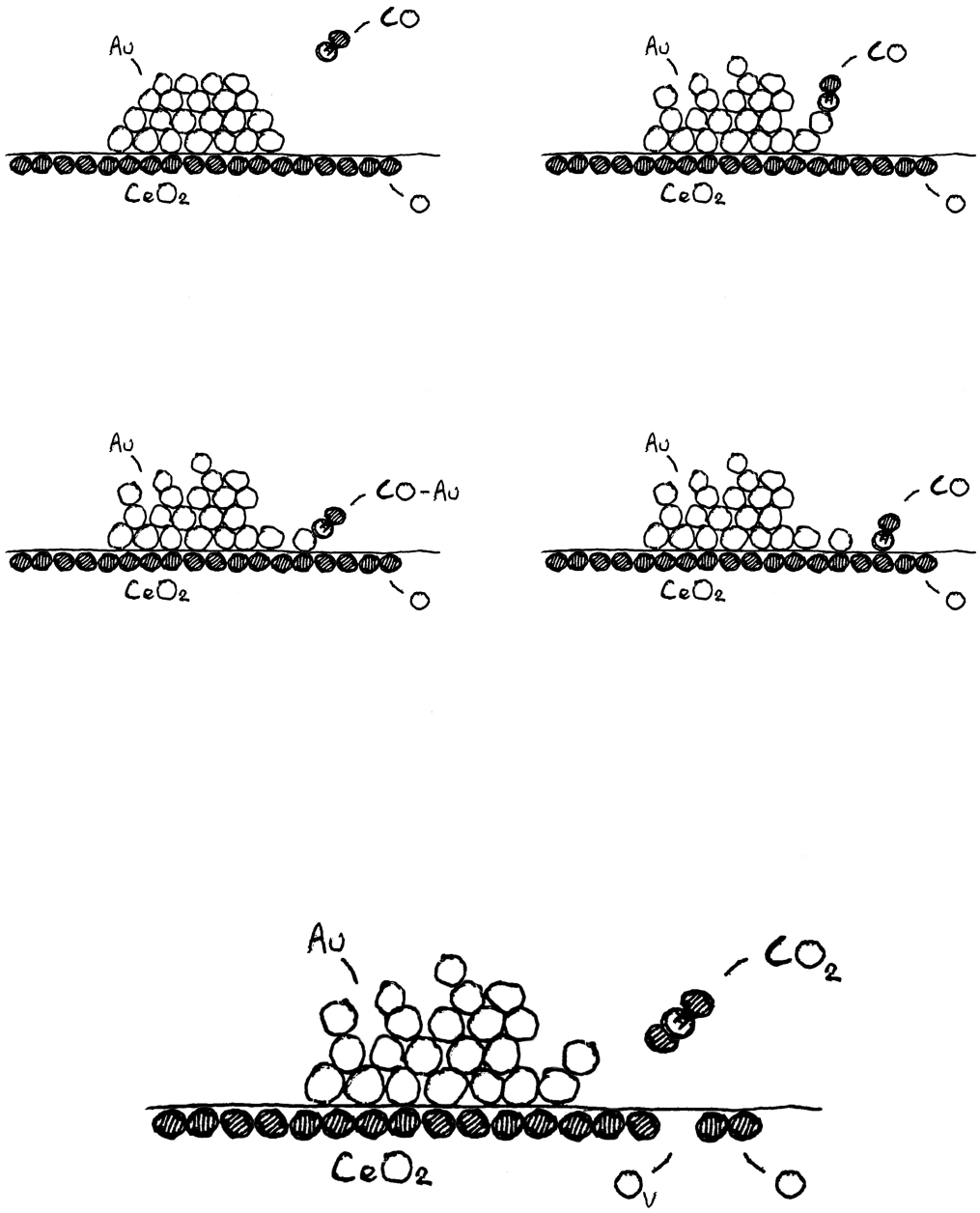

Figure 1.3: Dynamics of the redox process for small NPs. Exposing the NP to a CO/He environment activates the NP and the outermost Au ions begging moving. The CO molecule bounds to a gold ion on the NP surface. This Au-CO species moves from the NP surface to the Au/CeO_2 interface. Here the Au ion can briefly detach from the NP, until the CO molecule oxidizes to CO_2 on the ceria surface removing one O ion and leaving a vacancy. The single Au ion is then re-absorbed in the NP.

1.4. Goals

A lot of studies have been conducted to investigate the catalytic activity of ceria. XRD experiments have been conducted to follow the OS of Ce ions, since Ce^{3+} has an ionic radius larger than Ce^{4+}, an increase in lattice spacing higher than the simple one brought by heat expansion should be observed. The main limitations of this technique is that XRD is mainly surface sensitive and gives only an average picture of the surface behavior. Atomic Force, Scanning Tunneling and Tunneling Electron Microscopy (AFM, STM and TEM respectively) methods have been used to follow the behavior of the vacancies on ceria surface and of the Au NPs, from the dynamic of the surface and subsurface O vacancy, the localization of different OS species of Ce, to the movements of Au NPs. These techniques provide fascinating picture of the actual behavior of matter at its surface, but do not have access to the bulk.
To probe the amount of oxygen vacancies, X-ray Absorption Near-Edge Spectroscopy (XANES) experiments at the L_3 absorption edge of cerium has been exploited; since O vacancy formation and the reduction of Ce ions are bounded and occur at the same time [40, 41]. In the energy range of this edge, the mixing of d and f Ce^{3+} orbitals complicates the analysis of the spectral features [17, 42, 43]. Better resolution has been obtained in the High-Energy-Resolution Fluorescence Detection (HERFD) mode, but only partial information can be acquired this way.
In this thesis, a new method of following these changes is proposed. X-ray Raman Scattering (XRS) spectroscopy experiments have been conducted *in situ* for the first time, at the $N_{4,5}$ edge of cerium, on ceria pellets with Au NPs precipitated on the surface. We gain direct knowledge on structure of $4f$ electrons as we look at the $4d$ to $4f$ transition. With respect to X-ray Absorption Spectroscopy (XAS), XRS spectroscopy does not need high-vacuum condition to operate and can probe the bulk of crystals, giving insight on the bulk modification of the electronic structure of Ce ions, and therefore of the O vacancies. The complementary information obtainable this way should further expand our knowledge, and enlighten the role of hybridization between oxygen and cerium atomic states. The samples underwent CO treatments at increasing temperatures, while XRS measurements were taken.
The goal of this thesis is the study of the oxidation process happening on a $1\%Au/CeO_2$ sample in anaerobic condition with temperature ranging from 25 to 600 °C.
To build a reference for the experiments a theoretical model, *ab initio* DFT calculation and multiplet analysis have been performed with the Hilbert++ code to simulate the spectral features of the $N_{4,5}$ edge for Ce^{4+}, with electronic structure $[Xe]4d^0$, and for Ce^{3+}, $[Xe]4d^1$. The results are used to infer on the Ce^{3+}/Ce^{4+} ratio correlated to the O

vacancy concentration. XRD scans have been also conducted on the surface to follow the mean lattice spacing changes during the heating and the treatment to double check the generation of Ce^{3+} species.

1.5. Reflection on REE and the environment

The importance of REEs for high-technological application makes them a heavy component of the global market.The extraction of REEs is not an easy task. There are abundant reserves in mines of REEs, but their low concentration in the mined material, coupled with the costs of extraction and refinement render them relatively scarce [44]. The current extraction methods also involve environmental costs; radioactive minerals get extracted and a lot of polluting waste is produced in the process. The demand of REEs is continuously increasing world wide, and the issues of extraction should now be clear. Coupled with analysis on the environmental impact of dispersed ceria NPs [45], new methods for the extraction of these elements are understudy [46], and the possibility of separating REEs from end-of-life devices is showing promising results, in [47] is explained how Yujian Zhou et al. managed to recovered 85% of cerium of nearly 100% purity with a catalytic extraction and striping technique.
Better knowledge on the behavior of REEs could also help us understand them and replicate their properties in less demanding compounds.

2 | Multiplets and Matrix Elements
The rules of the game

2.1. Multiplet theory

In this chapter it will be shown how to study the electronic states of an ion introduced in a crystal. The theory as been reported following the work of Schülke in [48].

2.1.1. Atomic Hamiltonian for an isolated ion

The energy and the states of a system of an isolated ion are derived solving its Schrödinger equation

$$H\Psi = E\Psi,$$

where H is the Hamiltonian, Ψ is the many-body wavefunction, and E is the energy. With the infinite nucleus mass approximation, the Hamiltonian can be written as follow:

$$H = \sum_{i=1}^{N} \left(\frac{\mathbf{p}_i^2}{2m_i} - \frac{Ze^2}{\mathbf{r}_i} + \xi(\mathbf{r}_i)\boldsymbol{l}_i \cdot \boldsymbol{s}_i \right) + \sum_{i>j=1}^{N} \frac{e^2}{\mathbf{r}_{i,j}}.$$

$\mathbf{p}_i$ and m_i are the momentum and the mass of the i-th electron. Z is the nuclear charge number, taking into consideration how many protons are present in the nuclei, e is the electron charge, $\mathbf{r}_i$ is the position of the electron, $\xi(\mathbf{r}_i)$ takes into consideration the *strength* of the spin-orbit interaction, and $\boldsymbol{l}_i$ and $\boldsymbol{s}_i$ are the angular momentum and the spin of the electron. The last term takes into account the inter-electron interaction, it mixes the coordinates of different electrons as $\mathbf{r}_{i,j} = \mathbf{r}_i - \mathbf{r}_j$ and precludes the possibility of finding analytical solutions for systems with two or more electrons. The magnitude of this inter-electrons interaction is of the same order of the interaction between the electrons and the nuclei, and therefore it can not be treated as a perturbation. An approximated solution

can be found with the use of the mean field approximation. In this approximation, the electrons are considered to be moving independently from one another, inside an effective central field originated by the mean charge distribution of the other charges. The original Hamiltonian can be written as:

$$\begin{aligned} H =& H_0 + H_1, \\ H_0 =& \sum_{i=1}^{N} \left(\frac{\mathbf{p}_i^2}{2m_i} - \frac{Ze^2}{\mathbf{r}_i} + \langle \sum_{i>j=1}^{N} \frac{e^2}{\mathbf{r}_{i,j}} \rangle \right) = \sum_{i=1}^{N} \left(\frac{\mathbf{p}_i^2}{2m_i} - U(\mathbf{r}_i) \right), \\ H_1 =& \sum_{i=1}^{N} \xi(\mathbf{r}_i) \boldsymbol{l}_i \cdot \boldsymbol{s}_i + \sum_{i>j=1}^{N} \frac{e^2}{\mathbf{r}_{i,j}} - \langle \sum_{i>j=1}^{N} \frac{e^2}{\mathbf{r}_{i,j}} \rangle = H_{SO} + H_{elec}. \end{aligned}$$

where $\langle \sum_{i>j=1}^{N} \frac{e^2}{\mathbf{r}_{i,j}} \rangle$ is the average effect of the inter-electron interaction. We then define $U(\mathbf{r}_i)$ as the sum of the nucleus contribution and this average one brought about by the electrons. Now, H_0 can be used as an approximation of H to compute the states of the system described by

$$H_0 \Psi^0 = E^0 \Psi^0 \tag{2.1}$$

and H_1 can be treated as a small perturbation. The approximated many-body solutions to this equations are expressed with single electron wavefunctions ψ_k. Since the field applied is spherically symmetric, the ψ_k can be expressed with a radial, an angular, and a spinor component: $\psi_k = R_{n,l}(\mathbf{r}) Y_{l,m_l}(\theta, \phi)\ \chi_{m_s}$. Here n, m, m_l and m_s represent the the principal, the momentum, the magnetic and the spin quantum number of the electron, respectively. The solutions to the many body Schrödinger equation (2.1) have to be fully anti-symmetric and can be expressed through the Slater determinant:

$$\Psi^0(K_1, K_2, ..., K_N) = \frac{1}{\sqrt{N!}} \begin{vmatrix} \psi_1(K_1) & \psi_1(K_2) & ... & \psi_1(K_N) \\ \psi_2(K_1) & \psi_2(K_2) & ... & \psi_2(K_N) \\ ... & ... & & ... \\ \psi_N(K_1) & \psi_N(K_2) & ... & \psi_N(K_N) \end{vmatrix},$$

where K_i represent the spatial and spin coordinates of the electron with the quantum numbers $i = (n, m, m_l, m_s)_i$.

These functions can be used as basis for the perturbation terms of the inter-electron and the spin-orbit interaction. The nucleus electric field has as effect that of separating the energy levels of some of these many-body wavefunctions, depending on the electronic configuration of the electrons in the system. The resulting wavefunctions are characterized by the quantum numbers L and S, that represent the total angular and spin momentum. L and S are the result of the combination of the projection m_l, m_s on the quantization

axis of spin and angular momenta of all the electrons. Without taking into consideration the spin-orbit interaction, L and S are good quantum number, because they are conserved quantities and states with the same S and L have the same energy and are $(2L+1)(2S+1)$ times degenerate. The spin-orbit terms lift some degeneracy coupling these two quantities and the new conserved quantity is the total angular momentum J. The resulting states characterized by J can be expressed through the nomenclature ${}^{2S+1}X_J$[1] and are $(2J+1)$ times degenerate. A group of states characterized by the same ${}^{2S+1}X_J$ is called a *multiplet*.

2.1.2. Crystal field effects

The effects of a crystal in which a rare earth is introduced can now be examined. For $4f$ levels[2], the crystal field can be considered as a perturbation on the spin-orbit system. This is justified by the limited spatial extension of these orbitals, and by the relative screening that the full $5s$ shell electrons provide.
The interaction between one ion and the surrounding ones and its effects on the electronic structure can be modeled with an effective electrostatic field, the *crystal electric field* (CEF). The perturbation Hamiltonian can be written as:

$$H_{CEF} = -eV_{CEF}(r, \theta, \phi),$$

where V_{CEF} is a crystal field potential. This term has the same symmetry of the environment of the crystal in which the ions are placed. The original states were originated by a central field and were $(2J+1)$ times degenerate, the crystal field term should lift some of these degeneracies and therefore splits the multiplet levels. For a $4f^1$ electron as the one in Ce^{3+}, two SO multiplet states are available, the ${}^2F_{7/2}$ 8 times degenerate, and ${}^2F_{5/2}$ 6 times degenerate, separated due the spin-orbit interaction by roughly 250 meV. Taking into consideration the CEF, these multiplets further split into four and three degenerate *doublets*, separated by 50 meV, as depicted in Figure 2.1. These are the states that will be involved as final states of the X-ray Raman spectroscopy experiments that were conducted for this thesis.

[1] X takes on different letters according to the value of L, for L = 1, 2, 3, 4, .. X becomes S, P, D, F, ...
[2] A cerium atom with with configuration [Xe]$4f^1 5d^1 6s^3$, often takes on the oxidation states Ce^{3+} and Ce^{4+}, with electronic configurations [Xe]$4f^1$ and [Xe]$4f^0$, respectively.

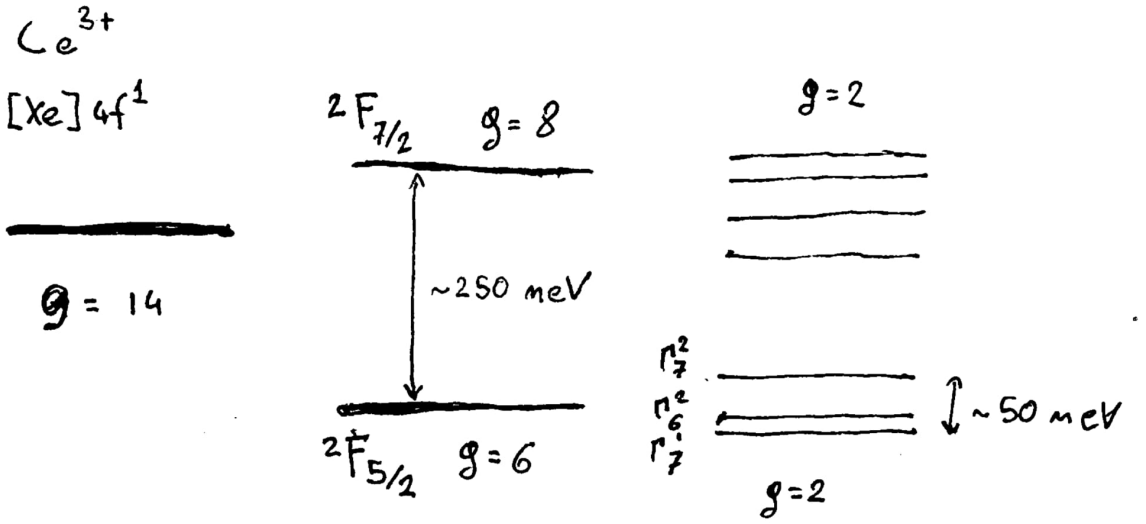

Figure 2.1: Multiplet energy configuration for a Cerium ion in crystal with oxidation state Ce^{3+}, the degeneracy is referred as g. On the left we have the original multiplet states, these are split into the two separate multiplets $^2F_{7/2}$ and $^2F_{5/2}$ by the SO interaction. Taking into account also the perturbations coming from the crystal field, the multiplet further split into the doublets on the right.

2.2. X-ray Raman scattering

X-ray Raman scattering is an inelastic phenomenon that can be used as a spectroscopy technique [48]. Photons interact with the sample and get scattered in the surrounding environment. Some of the energy is transferred to the electronic system and the outgoing photons have different energies and wavevectors with respect to the impinging one, see Figure 2.2. The electronic structure of the elements under investigation can be probed analyzing the change in the energies and wavevectors of the photons. The fantastic property of X-ray Raman spectroscopy is that we can obtain the same information that we would obtain in a soft XAS experiment. As it will turn out in the following, as long as the momentum transfer of the interaction is small, the matrix element of the interaction is the same of a simple absorption. This by itself is already remarkable, thanks to the use of the more penetrating hard x-ray we have much more bulk sensitivity, moreover it is possible to conduct experiments equivalent to the absorption ones to liquids and gasses since for hard x-ray it is no longer necessary to keep the sample under high vacuum conditions. One of the most particular features of x-ray Raman spectroscopy comes from the fact that when the momentum transfer is increased, by looking at the photons that are

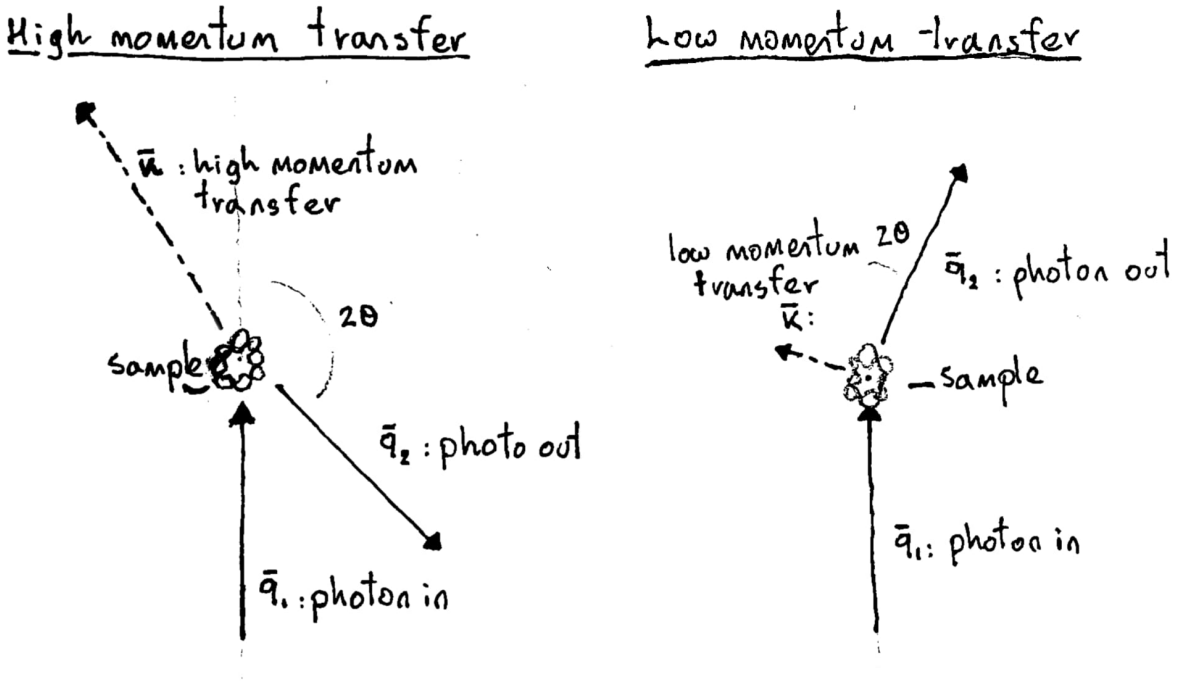

Figure 2.2: Schematics of the X-ray Raman inelastic scattering process. The incoming and scattered photons have a wavevector $\boldsymbol{k}$ and $\boldsymbol{k'}$, the momentum transfer $\boldsymbol{q}_{l,h}$ is equal to $\boldsymbol{k'} - \boldsymbol{k}$

scattered in directions with higher angles with respect to the in-photon direction, other terms of the interaction Hamiltonian prevail, and transitions that go beyond the dipole approximation become not only possible, but the relevant ones, opening up new spectral feature.

2.2.1. Matrix element

The interaction between the electromagnetic field of the incident x-ray beam and a charged particle as electrons can be derived by the kinetic energy operator $(\boldsymbol{p} - e\mathbf{A})^2/2m$, and it is described by the following Hamiltonian:

$$H_{int} = \sum_j \frac{e^2}{2mc^2} \boldsymbol{A}_j^2 + \sum_j \frac{e}{mc} \boldsymbol{p}_j \cdot \boldsymbol{A}_j, \tag{2.2}$$

$\boldsymbol{p}_j$ and $\boldsymbol{A}_j$ are the momentum of the j-th electron and the vector potential of the electromagnetic field [49]. The first term of this Hamiltonian, the one proportional to $\boldsymbol{A}^2$, is responsible for scattering process in a first-order perturbation treatment, whilst the

second term will contribute to the scattering in a second-order perturbation treatment, giving rise to a resonant scattering term. For the experiment presented in this thesis only the first term will be of interest. The interaction Hamiltonian can therefore be divided in to terms, $H_{int} = H_{i1} + H_{i2}$. With $H_{i1} = \sum_j \frac{e^2}{2mc^2} \boldsymbol{A}_j^2$, and using the *Fermi Golden Rule*, we can derive the following XRS double differential scattering cross section[3]:

$$\frac{d^2\sigma}{d\Omega_2 d\omega_2} \propto \frac{2\pi}{\hbar} \left|\langle f|H_{i1}|i\rangle\right|^2 \delta\left(E_f - E_i - \hbar\omega\right)$$

$$\frac{d^2\sigma}{d\Omega_2 d\omega_2} = r_0^2 \left(\frac{\omega_2}{\omega_1}\right) \sum_f \left| (\boldsymbol{e}_1 \cdot \boldsymbol{e}_2) \langle f| \sum_j e^{-i\boldsymbol{k}\cdot\boldsymbol{r}_j} |i\rangle \right|^2 \delta\left(E_f - E_i - \hbar\omega\right). \tag{2.3}$$

This cross section describes the interaction shown in Figure 2.2. The photon impinges on the target with $\boldsymbol{e}_1$, $\boldsymbol{q}_1$, ω_1, transfer some energy and is scattered back with $\boldsymbol{e}_2$, $\boldsymbol{q}_2$, ω_2. For the energy and momentum conservation principle, the photons transfer to the electron system the energy $\hbar\omega = \hbar\omega_1 - \hbar\omega_2$ and the momentum $\hbar\boldsymbol{k} = \hbar(\boldsymbol{q}_1 - \boldsymbol{q}_2)$.
Expression (2.3) can be written more concisely as:

$$\frac{d^2\sigma}{d\Omega_2 d\omega_2} = \left(\frac{d\sigma}{d\Omega_2}\right)_{Th} S(\boldsymbol{k}, \omega),$$

with $(d\sigma/d\Omega_2)_{Th} = r_0^2(\omega_2/\omega_1)(\boldsymbol{e}_1 \cdot \boldsymbol{e}_2)^2$ which is the Thomson scattering differential cross section, and $S(\boldsymbol{k}, \omega) = \sum_f \left|\langle f| \sum_j e^{-i\boldsymbol{k}\cdot\boldsymbol{r}_j} |i\rangle\right|^2 \delta\left(E_f - E_i - \hbar\omega\right)$ is the dynamic structure factor[4].
For low $\boldsymbol{k}$ the exponential term in the dynamic structure factor can be expanded as:

$$e^{-i\boldsymbol{k}\cdot\boldsymbol{r}_j} \approx 1 + i\boldsymbol{k}\cdot\boldsymbol{r}_j - (\boldsymbol{k}\cdot\boldsymbol{r}_j)^2/2 + \ldots. \tag{2.4}$$

When $\boldsymbol{k}\cdot\boldsymbol{r}_j \ll 1$, replacing (2.4) in (2.3), we obtain a term proportional to $\langle f|1|i\rangle = 0$ [5], and a dipolar term proportional to $\langle f|i\boldsymbol{k}\cdot\boldsymbol{r}_j|i\rangle$, that dominates over the subsequent terms. This term has the same dependence on the wavevector $\boldsymbol{k}$ and on the electrons position

[3]The cross section is, in a very simplistic sense, the area of the target particle of the transition. It is proportional to the square of the classical radius of the electron, r_0, and the rest bit takes into account the probability that a photon, with energy $\hbar\omega_1$ coming from the beam, has to change the state of the electron at position $\boldsymbol{r}_j$ from the initial state $|i\rangle$ to the final state $|f\rangle$, transferring it a momentum $\hbar\boldsymbol{k} = \hbar(\boldsymbol{k}_1 - \boldsymbol{k}_2)$ and the energy $\hbar\omega = \hbar(\omega_1 - \omega_2)$, when the photon is scattered in the solid angle $d\Omega_2$, with energy $\hbar\omega_2$. Since we have a lot of possible final states for various electrons, to obtain the total double differential cross section we need to perform the summation over all the final states and all the electrons involved.

[4]Now, all the information about the target are contained only in the dynamic structure factor

[5]It is always zero unless the initial and final state are the same, this would mean that nothing has happened though and so it is describing something that is really not interesting and we can forget about it.

$\boldsymbol{r}_j$ of an absorption cross section, described by the second term on the right hand side of (2.2), the same that describe the transition in XAS experiments, where a photon with wave vector $\boldsymbol{k}$ is completely absorbed by the system. Increasing the momentum transfer [6] the Taylor expansion breaks down and terms others than the first dipolar one become dominant. In this case it is more convenient to expand the vector potential in spherical harmonics

$$e^{-i\boldsymbol{k}\cdot\boldsymbol{r}} = \sum_{q=0}^{+\infty} \sum_{m=-q}^{q} i^k (2q+1) j_q(kr) C^*_{q,m}(\theta_k, \phi_k) \cdot C_{q,m}(\theta_r, \phi_r),$$

here the $j_q(kr)$ are spherical Bessel function of the q-th order, and k is the modulus of the exchanged momentum. The $C_{q,m} = \sqrt{4\pi/(2q+1)}Y_{q,m}$ are the normalized spherical harmonics, here is contained the dependence on the direction of the momentum. The initial and final state of the system are written as the product of one-particle wavefunctions, which are themselves expressed as the product of a radial function $R_j(r)$, and a spherical harmonic $Y_{q,m}(\theta_r, \phi_r)$. The term inside the bra-ket of (2.3) can therefore be written as:

$$\langle R_f(r) \cdot Y_{l_f,m_f}(\theta_r, \phi_r) | e^{-i\boldsymbol{k}\cdot\boldsymbol{r}} | R_i(r) \cdot Y_{l_i,m_i}(\theta_r, \phi_r) \rangle = \sum_{q,m} A_{q,m} I_{q,m}$$

with

$$A_{q,m} = i^k (2q+1) C^*_{q,m}(\theta_k, \phi_k) \langle R_f(r) | j_q(kr) | R_i(r) \rangle \tag{2.5}$$

and

$$I_{q,m} = \langle Y_{l_f,m_f}(\theta_r, \phi_r) | C_{q,m}(\theta_r, \phi_r) | Y_{l_i,m_i}(\theta_r, \phi_r) \rangle. \tag{2.6}$$

At this point, from (2.6) we can obtain the selection rules of the transition, which can be expressed with the Wigner 3j-symbols:

$$I_{q,m} \propto \begin{pmatrix} l_f & q & l_j \\ 0 & 0 & 0 \end{pmatrix} \begin{pmatrix} l_f & q & l_j \\ -m_f & m & m_i \end{pmatrix}.$$

This term does not vanish only when: $|l_f - l_i| < q < l_f + l_i$, and when $l_f + l_i + q$ is equal to an even integer. For instance, in the case of transitions involving a d and an f state, when $l_i = 2$, and $l_f = 3$ then, $I_{q,m}$ is different from zero only when $q = 1, 3$, and 5; these are respectively the dipole, octupole and trakontadipole transitions [50].
The radial matrix element in (2.5), $\langle R_f(r) | j_q(kr) | R_i(r) \rangle$, links the probability of a transition from $|i\rangle$ to a certain $|f\rangle$, to the modulus of the momentum transfer k. This matrix element is different from each order of the Bessel function j_q, and it has a maximum for

[6] This means that we look at photons that are scattered with higher angles with respect to the incoming photons. The difference between the incoming photon wave vector and the scattered photon wave vector gives the momentum transfer to the electron $\boldsymbol{k}_1 - \boldsymbol{k}_2 = \boldsymbol{k}$

different values of k. In particular, the maxima shift to higher values of k increasing the order q. At higher momentum transfer, the contribution to the spectrum will be given by higher order transition. Moreover, this matrix element is at its highest when the two radial function have the same principal quantum number. For this reason it is better to look at the $N_{4,5}$ edge, involving $4d$ and $4f$ states, than the $M_{4,5}$, which involve the $3d$ to $4f$ transitions [51].
Through x-ray Raman scattering it is possible to chose the momentum transfer of the transition and access also the transition over the dipole that would prohibited by normal XAS.

2.2.2. $|\,f\,\rangle$ and $|\,i\,\rangle$ for Ce

During the experiment performed for this thesis, the transition at the $N_{4,5}$ edge of Ce^{4+} and Ce^{3+} are probed. This edge of x-ray absorption involves the transition of $4d$ electrons into the $4f$ shell, completely empty for Ce^{4+}, and only partially empty for Ce^{3+}. The initial electronic configuration are therefore $[Xe]4f^0$ and $[Xe]4f^1$. Considering the Ce^{3+} case, once an electron has been promoted to the $4f$ shell, the energy configuration of the multiplets changes to a more complicated structure, schematically shown in Figure 2.3. For the Ce^{4+} species, an electron from the $4d$ orbital can be excited to one of the 7 multiplet states of the $4f$ empty orbital[7], so at most 7 different energy might be required to promote the electron; for Ce^{3+} instead, one electron is already present in one of the multiplet states shown in Figure 2.1, that have roughly the same probability of being occupied since their energies is really close to each other. The energy required now to add an extra electron, form $4d$ to $4f$, depends also on how two electrons arrange themselves in the $4f$ orbital. Having to take into consideration the spin of the electron as well this time, the available states are $7 \times 2 = 14$, so there are $14 \times 13 = 182$ different configurations, with different energies that can be absorbed to promote an electron from the $4d$ orbital to the $4f$ one.

[7]Here we do not take the spin into consideration

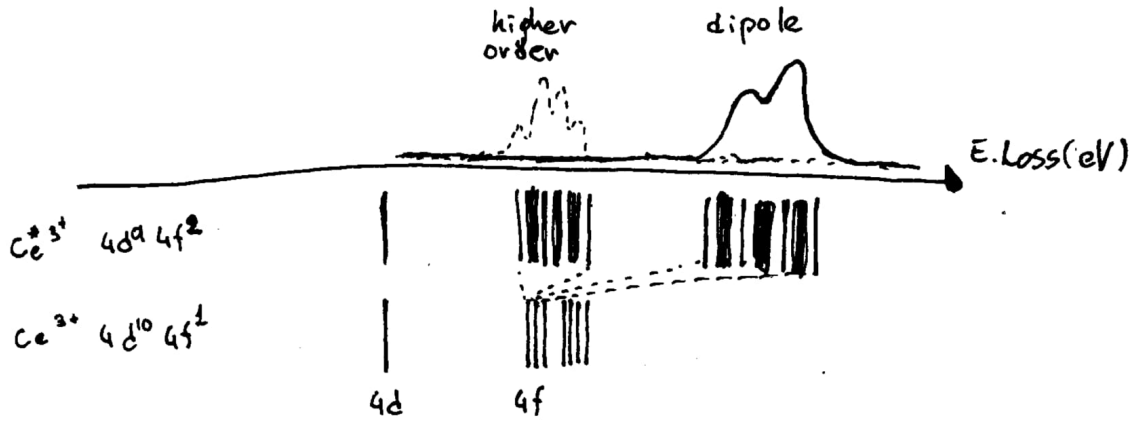

Figure 2.3: $4d^{10}4f^1$ to $4d^94f^2$ transition scheme for a Ce^{3+} ion. The lower vertical lines close to each others represent the energy levels of the system's duplets generated from the ${}^2F_{7/2}$ and ${}^2F_{5/2}$ SO multiplets. The vertical lines above represent the configuration of states for the excited system with configuration $4d^94f^2$. Above the black solid line is a schematic the X-ray Raman spectrum at the $N_{4,5}$ edge for low momentum transfer, and the dashed line for high momentum transfer.

3 | Experimental techniques and setup
Toys, tactics and playing field

Here we will describe a little more thoroughly the beamline, the used spectrometer and finally we will describe the experiment.

3.1. ESRF

The experiments and the analysis reported were conducted at the ID20 at ESRF, the European Synchrotron Research Facility. The ESRF is one of the most advanced synchrotron facilities in the world up to date, 2023, and the first third generation synchrotron in the world. ID stands for insertion device, at ID20 the radiation generates from three revolver undulators, with the choice between U35 and U32, where the numbers stand for the length of the period of the undulators in millimeters, with a brilliance of the order of 10^{20} photons/s mm^2 mrad^2 0.1% bandwidth in normal conditions [50], which means an average current of 200 mA in the ring. Further information on the functioning of synchrotrons can be found in literature [52].

3.2. ID20

The ID20 is one of the beamlines present at the ESRF (European Synchrotron Research Facility) in Grenoble, France. The main activities concern the study of matter through inelastic x-ray scattering. ID20 is equipped with a RIXS (Resonant Inelastic x-ray Scattering) spectrometer and a large-solid-angle XRS spectrometer. We will focus only on the latter since it is the one used for the experiments reported in this thesis.

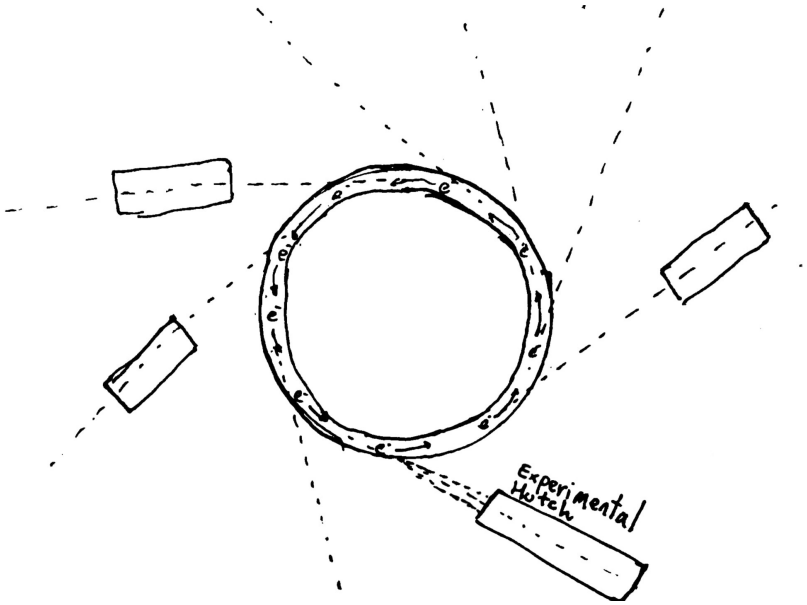

Figure 3.1: Drawing of a synchrotron seen from below, inside the ring are shown the electrons in motion, the dashed lines are the directions of the collimated beams and the boxes are the experimental hutch placed around the ring.

3.3. Large-solid-angle XRS spectrometer

The large-solid-angle XRS spectrometer installed at ID20 consists in six modular units mounted on a hemispherical structure around the sample site, shown in Figure 3.3. More detailed information on the instrumentation can be found in the paper at reference [50]. ID20 beamline uses a pre-monochromator consisting in two Si(111) crystals, it is cooled by liquid nitrogen to avoid thermal deformation due to the beam power. This pre-monochromator can be used alone or coupled with other post-monochromators [50]. For the experiment reported in this thesis we used the Si(111) pre-monochromator and a Si(311) channel-cut.

Downstream the beam is focused by a toroidal mirror on a secondary source, and then refocused on the sample on a spot size down to 8 μm $\times$ 16 μm. For this experiment the beam was focused on a spot size of 10 μm $\times$ 20 μm.

The analyzer crystals and the 2D detectors are located on a Rowland circle, working in a Johann configuration[1]. The spectrometer has six units containing each twelve analysing crystals and a detector[2]. The detector is mounted as close as possible to the sample in order to work in nearly back-scattering configuration; the resolution of the analyzer is pro-

[1]This means that the sample, the analyzer crystals and the detectors are all aligned on the surface of a virtual circle, called a Rowland circle. The light scattered from the sample hits the spherically bent crystals and is focused on the detectors.

[2]The detectors are single-chip Maxipix implementing a Timepix readout chip.

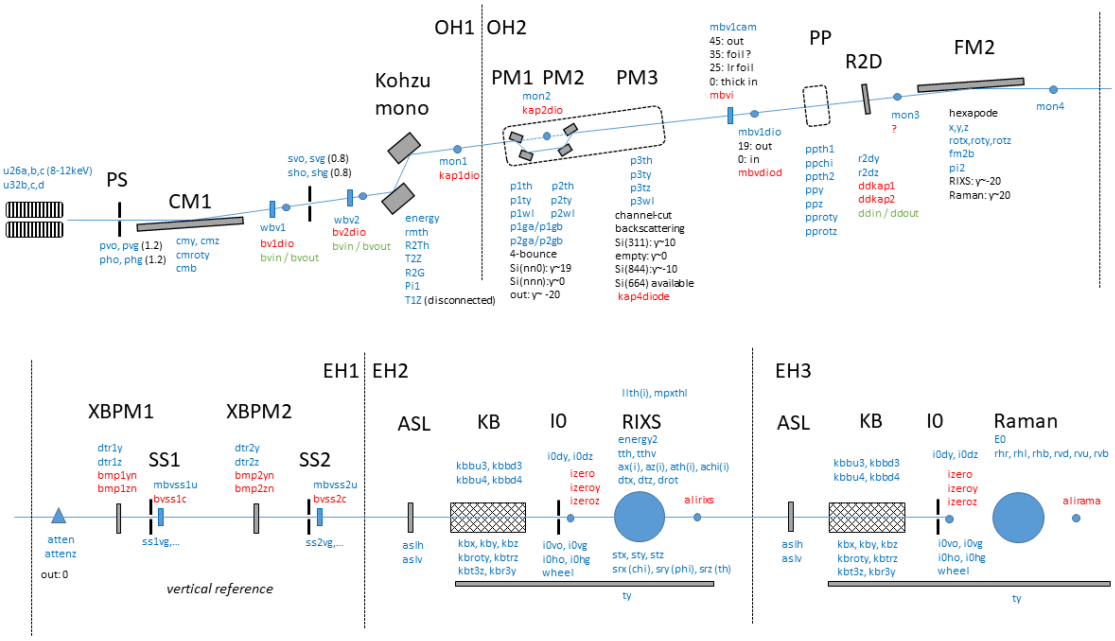

Figure 3.2: Optic schematics of the ID20 beamline at ESRF, the components are named by their mnemonic codes reported in the table below

portional to a term that goes as the cotangent of the reflection angle of the beam on the analyzer crystals, plus a term proportional to $1/sin^2\theta_r$, $(\Delta E)/E \propto Acot\theta_r + B/sin^2\theta_r$. Working in back-scattering configuration means that the beam scattered from the sample, when hitting the analyzer crystals, is Bragg-reflected back with an angle close as possible to $\pi/2$, where the $cot\theta_r \to 0$ and $1/sin^2\theta_r \to 1$, before hitting the detector, improving the resolution power.

These units can be arranged to form different angle with respect to the beam and the sample, by moving them on two semi-circumferences, allowing for the choice of different momenta transfer during the XRS experiment. These units take the names vertical down (VD) and horizontal left (HL) for the low momentum transfer, vertical up (VU) and horizontal right (HR) for medium momentum transfer and vertical back (VB) and horizontal back (HB) for backscattering experiment with high momentum transfer.

At ID20, multiple analysing crystals are available and can be chosen depending on the necessity of the experiment. They consist in spherically bent Si($nn0$) crystals. For the experiment reported the Si(660) crystals were used.

The interest of the experiment was the excitation spectrum of the sample; this allows for a degree of freedom in the choice of incoming energy of the photons, since the interest is only in the difference between the frequency of the incoming photons and the scattered one, $\omega = \omega_1 - \omega_2$. The experiment can be conducted keeping ω_2 fixed at 9.7 keV,

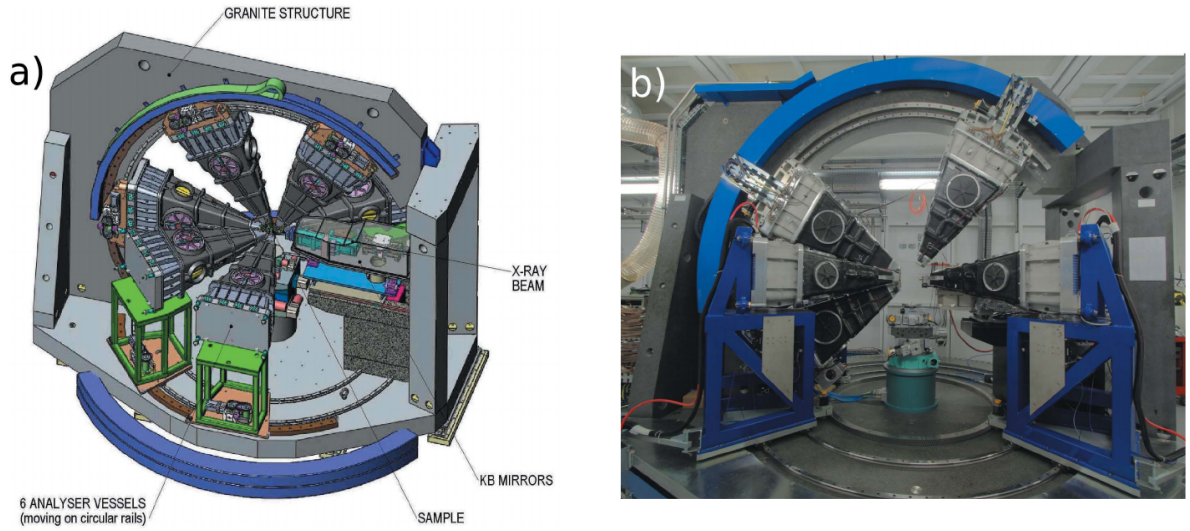

Figure 3.3: In a) a schematic of the large-solid-angle x-ray Raman spectrometer, here are shown the six units independently movable. In b) a photo of the spectrometer in the x-ray Raman experimental hutch at ID20.

and, scanning only the energy of the impinging beam on the sample, ω_1, the excitation spectrum can be obtained.

3.4. Experiment and sample preparation

3.4.1. Sample

The sample was prepared starting from a pellet of ceria Sigma-Aldrich, as received, Au NPs were precipitated on its surface. The concentration required was obtained through homogeneous deposition precipitation, using urea as precipitation agent [27, 35, 38]. Various pellets were left in a solution containing Au, for 16 hours at 80 °C under stirring. Then the pellets were dried and cleaned with water until no more of the urea's chloride ions were detected, using an $AgNO_3$ test. Among the pellets the one with 1 wt% Au NPs was chosen and used for the experiment ($1\%Au/CeO_2$). A picture of the sample, inside the sample chamber, is shown in Figure 3.4.
For the reference spectra of Ce when it is in the two different OSs, Ce^{3+} and Ce^{4+}, two pellets of pure ceria and cerium(III) sulphate Aldrich were used. Some XRS scans were performed at 25 °C with different scattering angles to obtain the XRS spectra at the $N_{4,5}$ edge for cerium in the oxidation states Ce^{3+}, in cerium sulphate, and Ce^{4+}, in ceria.

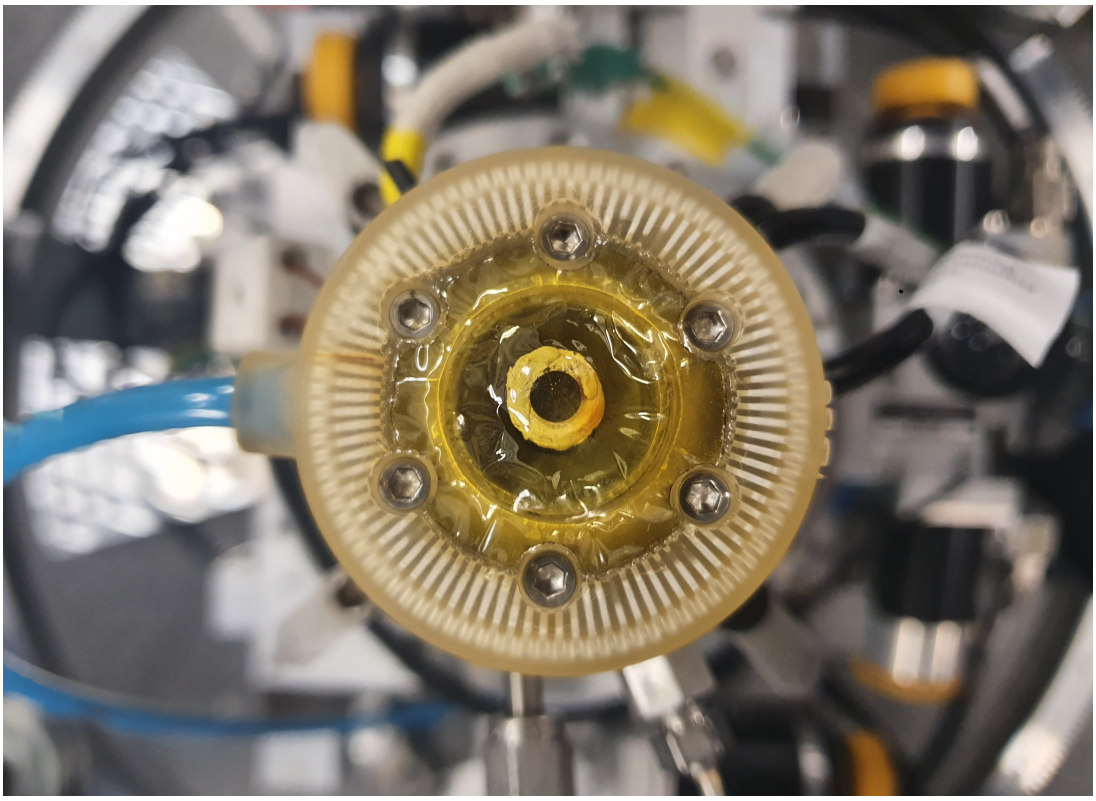

Figure 3.4: The black pellet in the center is the 1%Au/CeO_2 sample inside the sample holder during the X-ray Raman spectroscopy experiment. The white support on which the sample is mounted is the top part of the furnace heating the sample. The yellow structure is the sample holder composed of the air-tight transparent dome and the support.

3.4.2. Experiment

The sample has been encapsulated in a chamber, made by the sample holder and a transparent air-tight dome 3D printed at ESRF, mounted on a furnace, and placed in the center of the spectrometer forming a 10° angle with the beam. A picture of the setup is shown in Figure 3.5 The chamber was initially flushed with pure He at 20 ml/min[3]. To reduce the cerium in the ceria pellets from Ce^{4+} to Ce^{3+}, a mixture of He/1%CO was fluxed in the chamber for 120 minutes. The expectation was that ceria would donate some of the oxygen it stores to the gas oxidizing CO to CO_2. Afterwards the chamber has been fluxed with pure He for 30 minutes, and later a mixture of He/20%O_2 for 60 minutes. The data of the XRS experiment were collected *in situ*. The scans have been performed in the energy loss range of 0 to 700 eV with a step size of 1 eV[4]; later the energy loss range

[3]We kept always the total flux to this value for all the experiments

[4]Ce $N_{4,5}$ edge is located at lower energies, but together with this edge, also the O K edge has been probed, located between 520 and 590 eV.

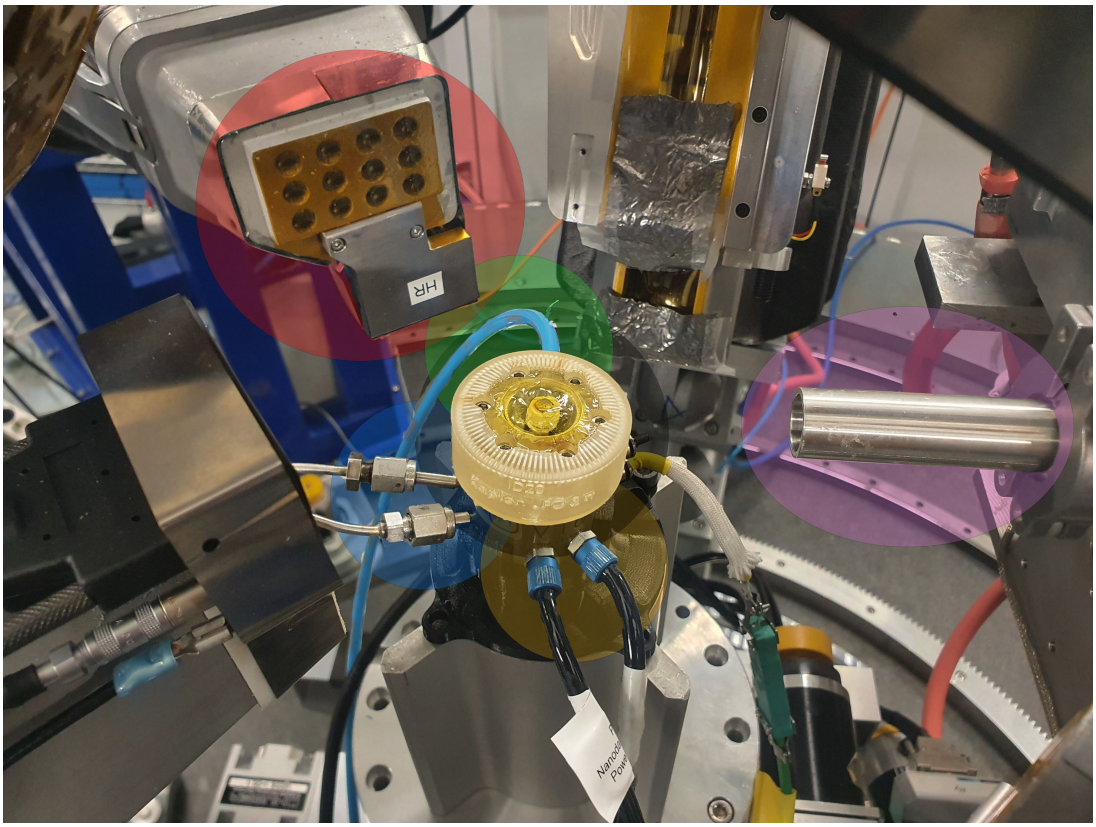

Figure 3.5: Sample environment at ID20 for X-ray Raman spectroscopy experiments. In the center of the picture, in the black circle, it is located the ceria sample used in the experiment. The yellow structure is the 3D printed air-tight dome. Attached to the dome are visible different cables: on the front, in the orange circle, the two black cables with a blue head control the furnace heating the sample; turning clockwise, the two silver cables in the blue circle, they are used to pump the 1%CO/He in and the reaction gas out; on the back, in the green circle, the blue cable is used to pump nitrogen on the dome to keep it cool, as the sample reaches temperatures of 600∼700 °C. Moving outside the sample environment, on the top left of the picture, in the red circle, the yellow holed plate is the entrance for the scattered beam hitting the twelve analysing crystals in the HR unit. The silver shape attached with HR written on it, underneath the HR unit, is the detector, placed as close as possible to the sample in order to work in back scattering configuration with the analyzing crystals and to leave enough room to operate on the sample itself. On the center right of the picture, in the purple ellipse, there is the metal tube from where the synchrotron beam comes and hits the sample.

between 95 and 150 eV has been probed with a step size of 0.2 eV. The overall resolution of 0.7 eV has been obtained by analysing the FWHM of the elastic scattering of some adhesive tape. To collect the data presented in this thesis, only the 24 analysing crystals of the VD and VB units were used. These units have been positioned at angles allowing for a momentum transfer of 3.5 and 9.5 $\pm$ 0.4 $Å^{-1}$.The collection time lasted 6 to 8 hours per sample, the temperature has been changed during the collection, starting from 25 °C and reaching gradually by variable steps 600 °C. At the same time to double check the results, XRD (X-Ray Diffraction) measurements have been performed. XRD has been used to measure the mean lattice spacing at the surface, as it is expected that, upon the reduction of more and more Ce from the OS 4+ to 3+, the lattice spacing increases; the Ce^{3+} has an higher ionic radius and therefore the we should find an overall lattice spacing increase higher than the one we should observe solely linked to the increasing of the temperature. The results of this measurements have been reported elsewhere, they helped to guide the advancement of this thesis as the results pointed in the same direction.

4 | Data analysis

VAR

The scope of the experiment was following the reduction process of ceria pellets with Au NPs precipitated on its surface, to quantify the ratio between two different oxidation states of Ce, Ce^{4+}/Ce^{3+}, through the analysis of the changes in the XRS (X-ray Raman Scattering) excitation spectra at the $N_{4,5}$ of Ce[20], whilst changing the temperature and the gas environment of the sample. The focus is on the use of these specific edges to quantify the ratio Ce^{4+}/Ce^{3+}. The data is collected by the 2D detectors mounted on the units. An image of the sample is generated on the detector where the intensity of the scattered beam is measured. The focal points of each analyzer crystals are positioned on different areas of the detectors. The implementation of 2D detectors has various advantages, firstly it is easier to use since the image of the sample does not have to be perfectly calibrated on a single spot but can hit any part of the detector, more images of the sample coming from different analysing crystals can be focused on the same detector. An other advantage of using a 2D detector is that a ROI (Region Of Interest) can be selected on the detector containing just the pixel with the signal from the sample, reducing this way unwanted features in the spectra. This feature comes particularly handy in case there is a complex sample environment, as the signal coming from sample holders, anvils, domes, etc. three examples are shown in Figure 4.1.

The images are pasted on a single figure ready for the analysis. At ID20 the Python library *XRStools* is implemented. This library allows for an easy extraction of the data and a preliminary analysis [53].

4.1. XRStools

The scans are uploaded and the image containing all 72 spots generated by the analysing crystals is presented. Here it is possible to select the ROIs of significance, in the case of this thesis just the 24 figures are taken into consideration, relative to the 12 analysing

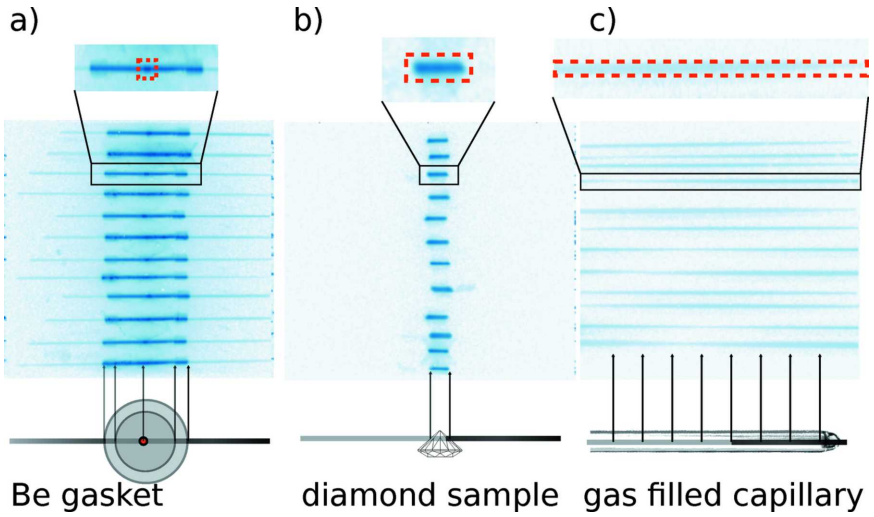

Figure 4.1: Three typical images that form on the 2D detector of the VU unit. The images are different for each sample, here are shown a) a sample contained in a diamond anvil, b) a diamond sample, and c) a gas-phase sample contained inside a long quartz-glass capillary. The area enclosed inside the red dotted line is an example of the choice for a significant ROI. [50]

.

crystals of the VD unit and the 12 of the VB unit. Once the ROIs have been selected, the signal from the same units are summed up and the X-ray Raman scattering spectrum is obtained. *XRStools* provides a feature with witch is possible to remove the background due to the Compton scattering. By choosing a region where the X-ray Raman scattering signal is low, a Pearson curve of the type VII is fitted to the data and subtracted from them[1]. Examples are shown in Figures 4.2 and 4.3.

A further refining of the data is possible at this point. Firstly a linear component of noise can be removed by fitting a straight line on the flat portion of the spectra before the X-ray Raman features, then the raw data were smoothed out using a Savitzky-Golay filter [54]. The window size has been set to 9 and the polygon degree approximating the data has been set to 3. The same sophistication that we applied to the data for the ceria coated with Au NPs, has been applied to the data obtain for the sample of pure ceria and cerium sulphate.

[1] At this point we should obtain a spectrum whose extremities present a flat behaviour and only the X-ray Raman scattering features and peaks are present. This procedure is more art than science as the choice of the initial guess for the curve severely impacts on the result and a certain sensibility has to be applied.

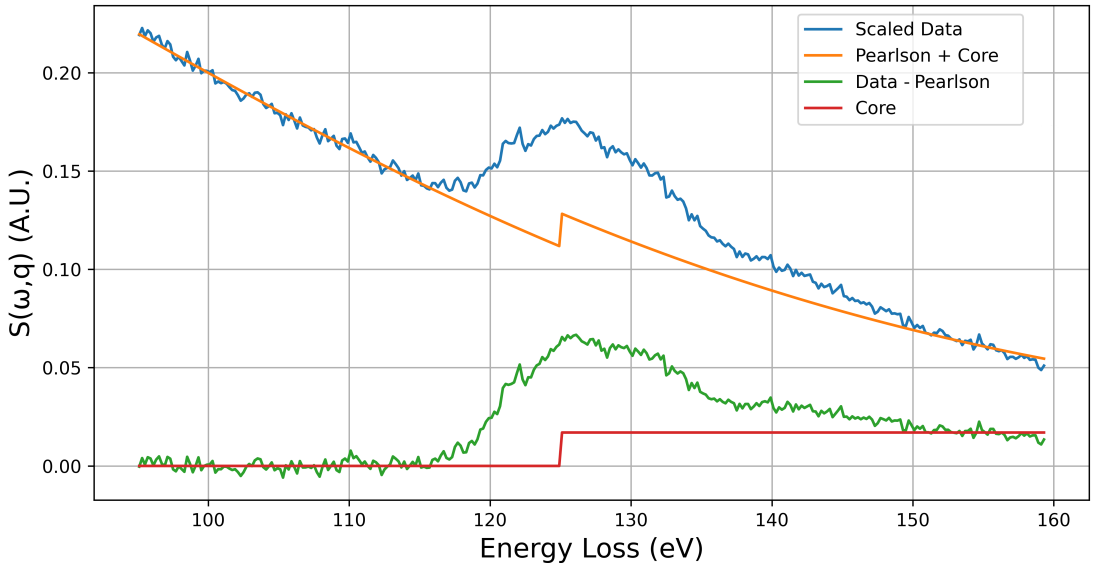

Figure 4.2: Spectra from the X-ray Raman scattering obtained at the $N_{4,5}$ of cerium(III) with a momentum scattering of $\boldsymbol{q} = 3.5$ Å^{-1}. The blue line is the spectra obtained from all twelve the analyzing crystals collected at the detector in the module VD. The green curve is the signal obtained after the removal of the Compton profile.

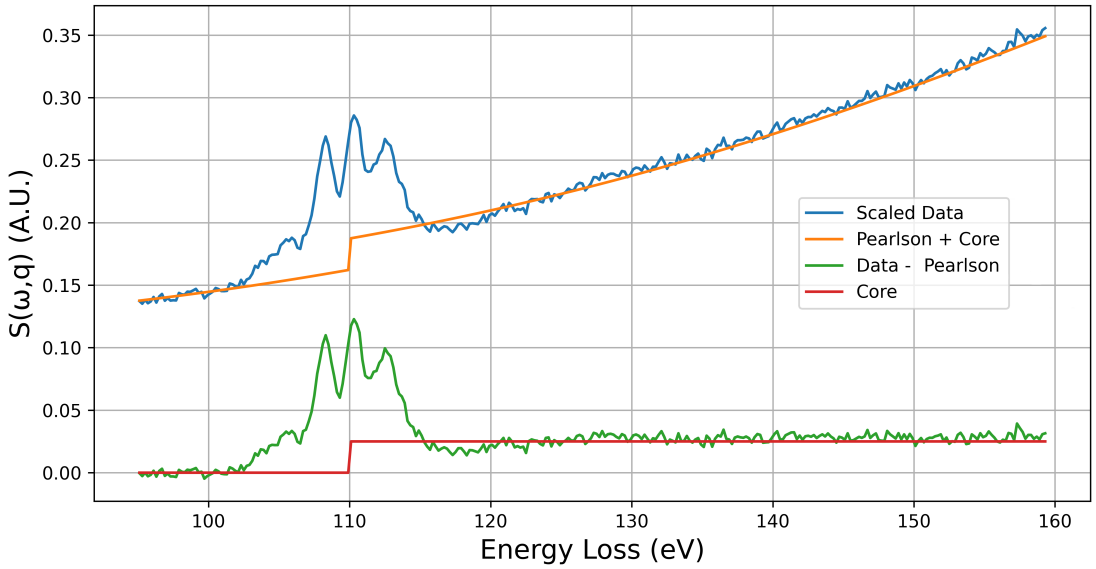

Figure 4.3: Spectra from the X-ray Raman scattering obtained at the $N_{4,5}$ of cerium(III) with a momentum scattering of $\boldsymbol{q} = 9.5$ Å^{-1}. The blue line is the spectra obtained from all twelve the analyzing crystals collected at the detector in the module VB. The green curve is the signal obtained after the removal of the Compton profile.

4.2. Experimental data

After the cleaning of the raw data we obtained the experimental spectra, ready to be interpreted. The spectra were plotted in the same graph to appreciate the changes. In the figure 4.4 are shown the changes on the spectra as we increase the temperature from 25 to 600 °C for low and high $\boldsymbol{q}$. In the low $\boldsymbol{q}$ spectra, it is observed that under the CO treatment the main peak at 133 eV, due to the Ce^{4+} component, decreases with the increasing temperature[2], while the shoulder at 125 eV, before the peak at 133 eV, broadens gradually with the CO treatment. This is coherent with the an increasing Ce^{3+} component. For the spectra obtained at high $\boldsymbol{q}$, during the treatment, the peaks at 112 eV and 108 eV also decrease, and an evident extra peak at 110 eV appears between the 108 eV and 112 eV peaks. The feature before 108 eV also undergo some changes, increasing the temperature the small peak at 106 eV increases slightly and the spectrum broadens on the left end of the pre-edge features.

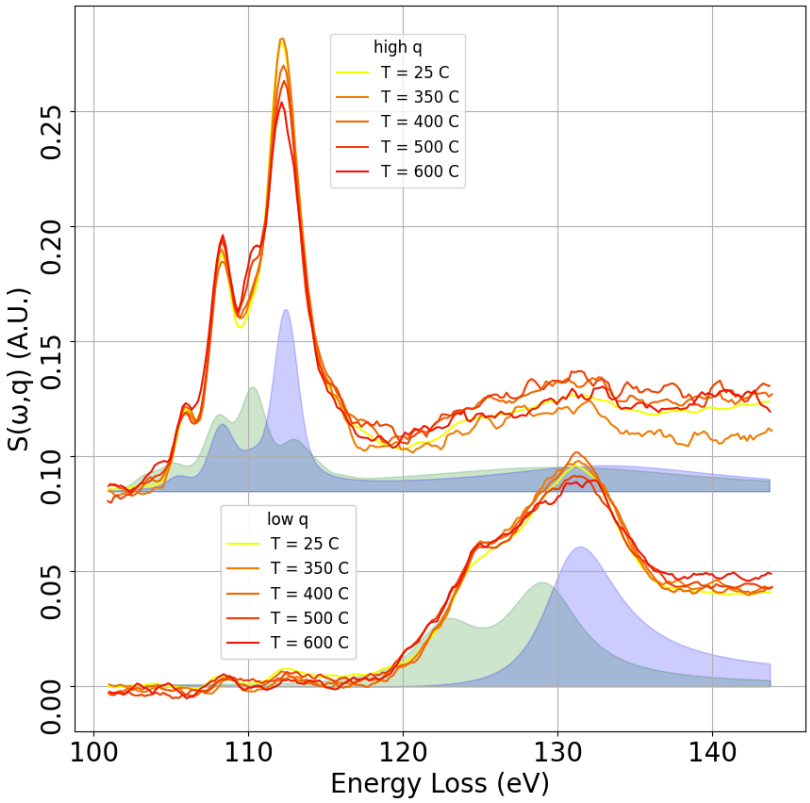

Figure 4.4: This are the experimental spectra obtained after the analysis. The green and purple shaded area below the curve are the simulated spectra for Ce^{3+} and Ce^{4+} respectively.

[2]This start happening already at 150 °C, which is lower than the temperature needed to observe the same behavior in ceria samples without Au NPs deposited on them

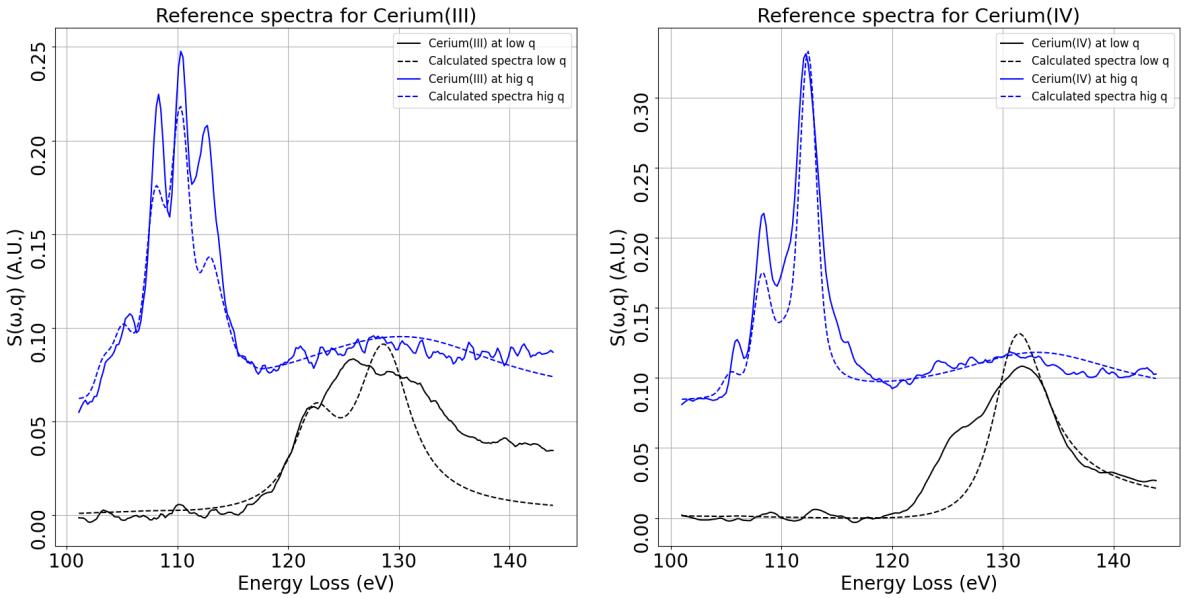

Figure 4.5: On the left the black and blue solid lines reported are the X-ray Raman scattering spectra of cerium(III) sulphate, $Ce_2(SO_4)_3$, for low and high momentum transfer, respectively. The dotted line are the calculated spectra using Hilbert++ for cerium in the oxidation state Ce^{3+}. On the right the spectra reported are the one for pure ceria(IV) Aldrich, CeO_2 the dotted lines are also the calculate spectra for cerium in oxidation state Ce^{4+}.

The experimental spectra obtained from the ceria sample and the cerium sulphate sample, at room temperature under aerobic conditions, are shown in Figure 4.5, both for low and high $\boldsymbol{q}$. These latter two spectra has been used to calibrate the simulated spectra obtained using the Hilbert++ code, developed at ESRF by A. Mirone [55, 56]; discussed in the next chapter.

5 | Results

Scoreboard

Here the results of the analysis conducted on the data are presented. Plotting together the spectra that were obtained experimentally with the one obtained through simulations allows to better understand the behavior of system.

5.1. Hilbert++

Hilbert++ is the code used to compute the multiplet spectra. With Hilbert++ it is possible to reproduce the q-dependence of XRS spectra with good agreement with the experiments. The code does so by calculating the dynamic structure factor $S(\boldsymbol{q}, \omega)$ of the sample, when the energy loss of the impinging photons is $\hbar\omega$ and the momentum transfer $\boldsymbol{q}$. The code was used because it reproduces well the excitations of core-to-$4f$ electrons in REEs. This code is able to take into account the environment effects of neighbouring ions to the absorbing one, and differently from similar codes that achieve the same good results, (through *ab initio* condition) it does not require a specific symmetry group for the crystal. This aspect makes it more versatile, but also more resource hungry, nevertheless, modern computer should be able to handle the computation power required[1]. The code is rigorously explained on a couple of papers reported in the bibliography, the earlier [56] and the more recent [57]. The dynamic structure factor of the multiplet structure is calculated for the central absorbing ion, using a DFT-relaxed structure. It has been used to calculated the spectra contribution to the complex case of ceria with Au NPs precipitated on its surface, at different temperatures by summing the spectra of cerium in the oxidation states Ce^{4+} and Ce^{3+}. The $N_{4,5}$ edge and pre-edge structure of cerium was used to study the sample, involving the excitation of core electrons from the $4d$ to the $4f$ orbital. In the simulations an ion of cerium has being placed in the center of a cubic lattice surrounded by eight oxygen ions. Four simulations have been ran: the transition

[1] Some simulation were run on my personal computer as well, which mounts a *simple* Intel Core i7 processor and a 16 GB RAM; the computation for a single simulation took roughly one minute.

of interest for cerium has been specified by typing in the input of the code the following:

```
transition = "4d4f"
atom = "Ce".
```

The oxidation state is specified by changing the value of the variable `occupancy` from `1` for Ce^{3+} to `0` for Ce^{4+}, the position of the neighbouring ions is specified in the `bonds` list, while the momentum transfer $\boldsymbol{q}$ is controlled through the variable `q_exp`, set at `9.5` $Å^{-1}$ for high momentum transfer and `3.0` $Å^{-1}$ for low momentum transfer:

```
occupancy = 1 #0
bonds = [
          [-1.352800,-1.352800,-1.352800],
          [-1.352800,-1.352800,1.352800],
          [-1.352800,1.352800,-1.352800],
          [-1.352800,1.352800,1.352800],
          [1.352800,-1.352800,-1.352800],
          [1.352800,-1.352800,1.352800],
          [1.352800,1.352800,-1.352800],
          [1.352800,1.352800,1.352800]
 ]

vc_d0 = 0.0
vc_d1 = 0.0
vc_f0 = 0.02
vc_f1 = 0.01
vc_g0 = 0.0
vc_g1 = 0.0

de = 0.001

q_exp = 9.5 #3.0

e_step_target = 0.05.
```

The `de` variable sets the energy range from the lowest energy eigenstates of the ground state that are considered for the spectra, the `e_step_target` variable sets the width of the

dynamic form structure peaks, while the `vc_xx` terms are empirical parameters for the crystal field that the Hilbert++ code uses in the Hamiltonian of the system to compute its multi-particle states. The first letter after `vc_` identifies the orbital affected by the crystal field, whether d, f, or g; the number identifies with `0` the orbitals aligned with the quantization axis, and with `1` the ones perpendicular to it. These parameters can be obtained through other *ab initio* codes, as the Wannier90 code, or through empirical values obtained with experiments. The one reported are used for the crystal field contribution to the Hamiltonian reported in [57]. The spectra obtained with Hilbert++ have been shifted in energy to match the peaks position obtained experimentally, then they have been convoluted with a Fano resonance line shape functions to reproduce the broadening due to the life-time of the excited state, and the broadening due the experimental setup. These functions are also used to reproduce an asymmetric broadening effect due to the interaction of confined quantum systems with the continuum, as is the case for the excitations happening at the $N_{4,5}$ edge of Ce. The results of this process are shown in Figure 4.5. There we can see how the computed spectra, depicted by the dotted lines, have been shifted in energy to match the peaks position of the experimental spectra. Later the computed spectra underwent the broadening process.
These computed spectra are the result of Hilbert++ simulations, the shift and the broadening have been done *by hand*, choosing the best parameters for the shift and for the convolution that matched at best the experimental data. In the future a more precise, and/or automatic way to do so could be developed. The result obtained are nevertheless in good agreement with what is already known in literature.
The spectra obtained from the data of the ceria sample has been used as reference for the spectra of the simulated Ce^{4+}, the one obtained with the cerium sulphate sample has been used for Ce^{3+}.
This simulation reproduce well the experimental results. A further refinement of the simulation can be obtained taking into the account the hybridization effects of the oxygen ions $2p$ orbitals with the cerium $4d$ orbitals. In the code shown above some extra parameters need to be added:

```
28   max_hoppedA = 1 #0
29   E_hopperA = -2.0+4.554839e+01
30
31   relative_E_hopperA = 3.0.
```

Here the `max_hoppedA` defines how many electrons are we allowing to to move from the ligand orbitals to the open shell, `E_hopperA` is a parameter which defines energy for which

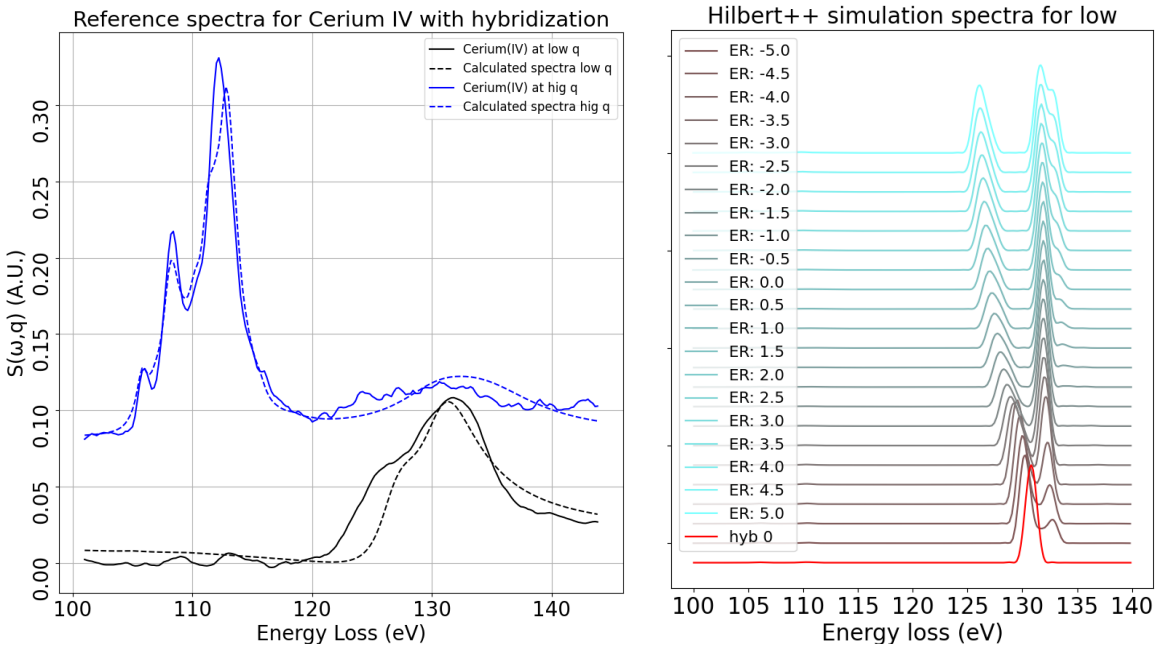

Figure 5.1: On the left: as in Figure 4.5, but the dotted line are the calculated spectra obtained taking into consideration the hybridization of the atomic orbitals of Ce and O. On the right: raw calculated spectra obtained from the Hilbert++ code before the convolution with a Fano function. The ER is the `relative_E_hopperA` parameter The various spectra are shifted in intensity of some arbitrary step to show the variation.

an electron from the central atom jumps to the ligand. If not defiened, the code automatically searches for this parameter and then it generates and saves the value on the neutrality_convergence.txt file; to skip the search after the first time, we can manually insert the value of this parameter reading the neutrality_convergence.txt file. The parameter `relative_E_hopperA` defines an arbitrary off-set to the variable `E_hopperA`, which can be used to fine tune the hybridization and test its effect on the spectra[2]. These new spectra have been calculated and are shown in 5.1.

5.2. Location

As explained in the literature [58] and seen in the reference spectra of cerium sulphate presented in 4.5, cerium in the oxidation state Ce^{3+} has an electronic configuration of

[2]To set the `relative_E_hopperA` variable to an high negative value is equivalent to say that the electron can not hop from the central ion to the ligand as the energy to do so is too high, in fact the left graph of Figure 5.1 shows that for higher and higher ER, which is the `relative_E_hopperA` parameter, the spectra are more and more similar to the spectrum without hybridization

[Xe]$4f^1$, and presents two peaks at the $N_{4,5}$ edge for the giant dipole, one at 120 eV and one at 125 eV. Calculation performed for Ce^{4+}, in configuration [Xe]$4f^0$, should present just one peak at the same edge. It is observed that at the beginning of the CO treatment at room temperature, 1%Au/CeO_2 presents two peaks, one at 124 eV and one at 133 eV, indicating that already at low temperature there is a Ce^{3+} component in the ceria sample. As shown in Figure 5.2, the CO treatment changes the spectra of ceria as the temperature is increased. At low momentum transfer, just the dipole giant resonance is visible in the spectrum; some changes are noticeable while the CO treatment is going on. The shoulder at 125 eV becomes slightly more pronounced as the peak at 133 eV decreases. The non-dipole multiplet structure, manifesting in the pre-edge features, is highly sensitive to the treatment. Increasing the momentum transfer, the contribution of the dipole component becomes practically unnoticeable and the spectra is dominated by the non-dipole transitions. During the treatment, increasing the temperature a peak arises at 111 eV while the one at 113 eV decreases. The spectra also broadens on the low energy loss end.
While the reduction of the sample cerium ions takes place, some electrons hop from $2p$ orbitals of the oxygen ions to the cerium $4f$ orbitals. The cerium ions involved change the oxidation state from Ce^{4+} to Ce^{3+} changing their electronic configuration from $4f^0$ to $4f^1$. The sensitivity of X-ray Raman spectra to the electronic configuration of the sample allows to follow this change in the sample. The calculated spectra for these two oxidation states have been used to quantify the ratio Ce^{4+}/Ce^{3+} in the sample. As shown in Figure 5.2 the weighted sum of the calculated spectra reproduces quite well the behavior of the experiments at high momentum transfer $\boldsymbol{q}$, the weight can be used to extract the amount of each component. At low momentum transfer $\boldsymbol{q}$, the calculated spectra reproduce less the experimental behavior. Already at low temperature a shoulder forms before the expected peak at 133 eV. This could be justified by a higher Ce^{3+} component present in the sample, but this leads to incoherent quantification of the ratio Ce^{4+}/Ce^{3+} between the experiment at low $\boldsymbol{q}$ and high $\boldsymbol{q}$, which is not possible.

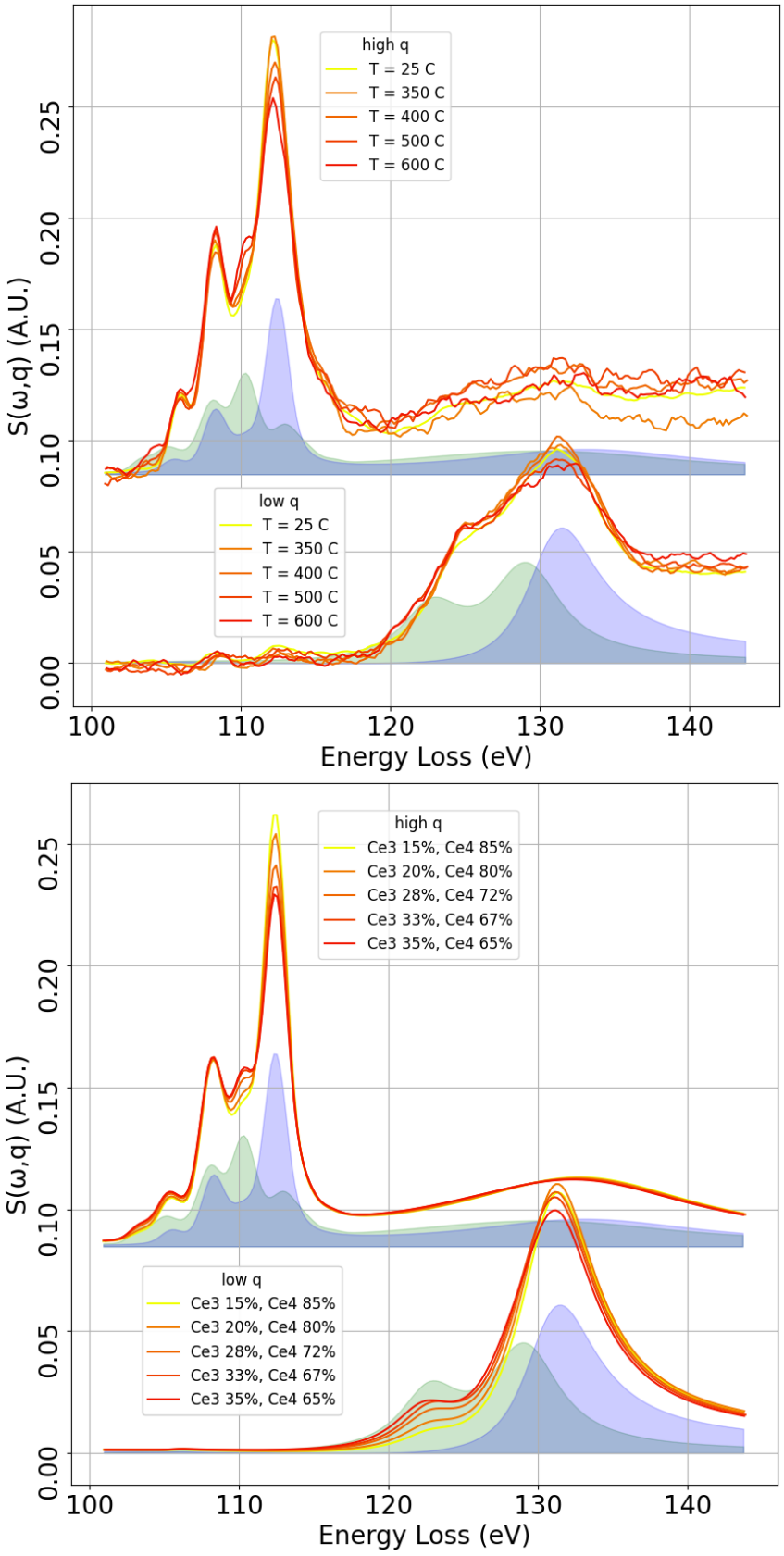

Figure 5.2: These are the experimental (on the right) and simulated (on the left) spectra obtained after the analysis. The shaded areas below the spectra are the calculated spectra for the two contribution coming from Ce^{3+} in green and from Ce^{4+} in purple. It can be observed that the simulations reproduce well the behavior of the experimental spectra.

The hybridization of oxygen $2p$ orbitals and cerium $4f$ orbitals could be considered to explain this behavior. The O $2p$ orbitals and Ce $4f$ have similar energies, and therefore some hybridization of the two might take place.
In [59], through Angle-Resolved Photoemission Spectroscopy ARPES experiments, it has been shown that there is some contribution of the empty $4f$ orbitals to the valence band of CeO_2. The empty $4f$ atomic orbital hybridize with the O $2p$ atomic orbitals. In the case of completely reduced ceria, or c-Ce_2O_3[3], this hybridization was not observed.
We have then run some simulations using the Hilbert++ code taking into consideration this hybridization to compute the spectra of cerium ions in the oxidation state Ce^{4+} [61] and electronic state $[Xe]4f^0$ for high and low momentum transfer.
At low $\boldsymbol{q}$, a second peak appears before the one placed at 133 eV, while at high $\boldsymbol{q}$ there are less changes. This is coherent with the shoulder found before at the dipole transition, as shown in the Figure 5.1, and with the fact that at the multipole transitions, the calculated spectra without hybridization was already close to the experimental results.
Even without hybridization, some features are already evident. In the figures 5.3 and 5.4 are shown the changes in the spectra for low and high $\boldsymbol{q}$ at 25 and 600 °C.

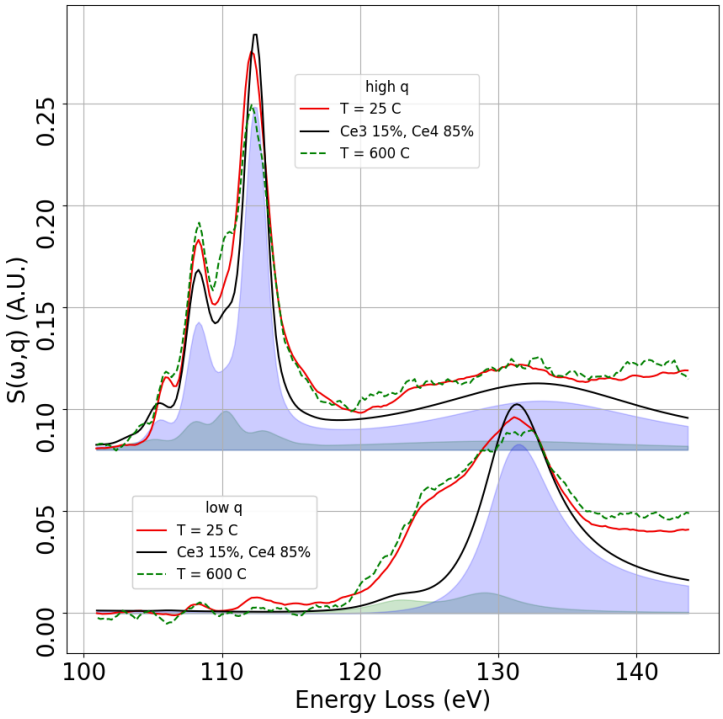

Figure 5.3: The red line is the experimental spectrum we obtained at 25 °, the black line are the calculated $S(\omega,\boldsymbol{q})$. The shaded areas underneath the curves are the contribution with which the two kinds of cerium gives to the total calculated spectrum. The green dotted line is the experimental spectrum for the same sample at 600 °C. Already at low temperature a little component of the Ce^{3+} is need to reproduce the experimental spectra

[3]By c-Ce_2O_3 it is meant completely reduced ceria holding its FCC fluorite structure, [60]

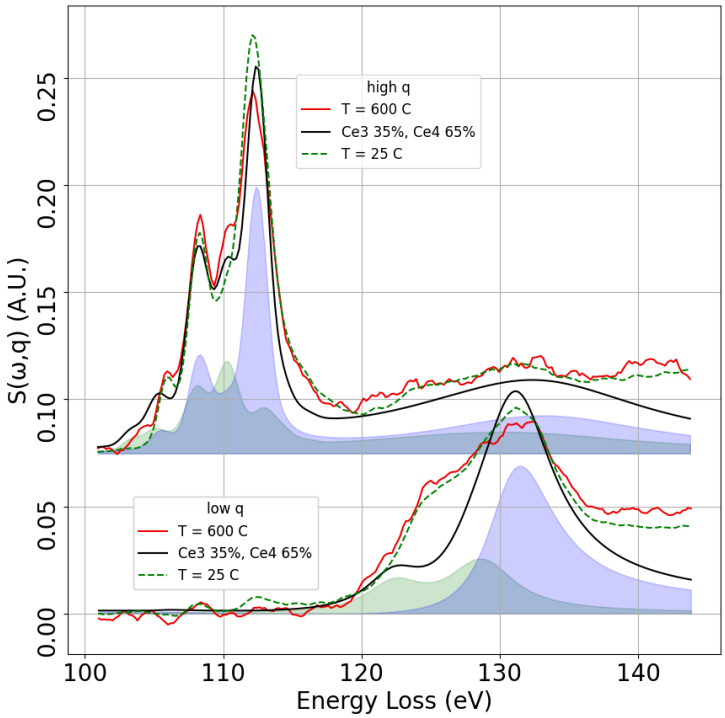

Figure 5.4: The red line is the the experimental spectrum obtained at 600 °, the black line are the calculated S(ω,$\boldsymbol{q}$), here the shaded are are still the contributions from the different oxidation states of cerium. The weights that they have are different with respect to the 25 ° case.

5.3. Quantification

After this considerations, keeping in mind the goal of the experiment, the next step has been to overlap the spectra obtained from the 1%Au/CeO_2 sample at different temperature with a weighted sum of the two reference spectra $S_{calc,Ce^{3+}}$ and $S_{calc,Ce^{4+}}$ as follows:

$$S_{calc} = w_{Ce^{3+}}\ S_{calc,Ce^{3+}} + w_{Ce^{4+}}\ S_{calc,Ce^{4+}}$$

with $w_{Ce^{3+}} + w_{Ce^{4+}} = 1$ [4]. The weights have been chosen to match the experimental results. It is interesting to quantify how much Ce^{3+} is present in the sample. Using the reference computed spectra for Ce^{3+} and Ce^{4+}, a mixed species spectra have been obtained. A weighted sum of the two references have been done, where the weights also represent the fraction of each species present in the sample. The weights have been therefore calibrated at each temperature in order to match at best the mixed species calculated spectra to the experimental one. Following this procedure we obtained that, with respect to the sample of pure ceria, at low temperature, 1%Au/CeO_2 has already a Ce^{3+} component of 15%. The higher concentration of Ce^{3+} in non defective ceria with Au NPs deposited on the surface was predicted, since the generation of a Schottky junction at the metal/metal-

[4]These weights represent the ratio of different oxidation of cerium in the sample, we'll see later in the chapter Results chapter that throughout the experiment, as the ceria reduces, the ratio of Ce_{3+} increases at the expenses of Ce_{4+}

oxide interface transfer some electrons from the metal to the support, reducing some Ce ions. Nevertheless a 1% coverage of the ceria surface does not justifies ratio of 15%. This indicates that the Au NPs play an important role on the capacity of cerium material to act as catalyst at low temperature. Increasing the temperature, a bigger and bigger ratio of the Ce^{3+} reference spectra is needed to match the experimental one, indicating a larger proportion of this species in the sample, and therefore an higher catalyst activity. After the CO treatment, at 600 °C, the the amount of Ce^{3+} increases up to 30∼35% of the total.

6 | Conclusion

After match

For the first time *in-situ* XRS measurements at the cerium $N_{4,5}$ edge have been performed to follow the reduction of Ce^{4+} to Ce^{3+}. This method can be used to study the oxygen vacancy formation and concentration on ceria based materials and deepens the knowledge on the electronic properties of this REE oxide.

6.1. The $N_{4,5}$ edges and pre-edges

We have shown how the analysis conducted on the excitation spectra at the $N_{4,5}$ edges and pre-edges of Ce can be effectively used to quantify the ratio of Ce^{3+}/Ce^{4+} in the ceria sample. While the spectra obtained at low momentum transfer $\boldsymbol{q}$ are slightly more difficult to interpret because of the broader peaks and the less differences between the two species, the high momentum transfer spectra show much clearer changes. The narrower peaks at high $\boldsymbol{q}$ are due to the fact these peaks are less affected by the interaction of the electrons with the continuum, which instead broadens the spectral features. Nevertheless, already at low $\boldsymbol{q}$ some conclusion on the amount of the Ce^{3+} can be drawn, showing the potentiality of this edge to probe the materials properties.

6.2. Gold Role

The ceria sample covered with Au NPs shows good catalytic properties for the the oxidation of CO into CO_2. As widely explained in literature [6], for pure ceria a complete conversion of the CO takes place at temperature close to 600 °C, in this thesis it is shown how Au NPs precipitated on the surface allow for the reaction to start at lower temperatures, already at 150 °C, with respect to the pure ceria samples. In particular, the Au ability to adsorb the CO molecules at higher temperature and lower partial pressure of the gas allows to obtain a conversion at lower temperatures with respect to pure ceria.

The overall sharpness of the spectral features is not affected, and thus the Au does not improve the information that can be extracted analyzing the sharp $N_{4,5}$ edge and pre-edge features. The use of noble metals to improve the CO oxidation process shows promising results for future technology applications.

6.3. Hybridization effects

The effect of hybridization on the spectra has not been previously discussed for the $N_{4,5}$ edge. It emerged especially from the low momentum transfer spectra that a model taking into consideration a partial hybridization of the oxygen and cerium(IV) ions atomic orbitals is needed. In their study, through multiple body physics and DFT simulations of Ce^{3+} and Ce_2O_3, Herper et al. concluded that a strong hybridization is found in the CeO_2 giving the $4f$ states highly itinerant nature. For Ce_2O_3 the states are more localized but maybe less than previously though, also considering c-Ce_2O_3 which conserves the fluorite configuration with respect to the hexagonal crystal structure of Ce_2O_3. For Ce_2O_3 the $4f$ electrons are even more localized [61]. The same results were also found in ARPES experiments conducted by Duchon T. et al. [59]. Even in the groundstate where the $4f$ cerium orbital is empty, there is a contribution of this orbital to form a covalent bond hybridizing with the $2p$ oxygen bands. They also found out that the $4f$ state is more localized for FCC fluorite c-Ce_2O_3 than it is for the Ce_2O_3 with hexagonal structure.
Even with the hybridization simulations, not all the shoulder is justified, suggesting that already at room temperature a certain amount of Ce^{3+} is already present, and therefore some oxygen vacancy as well.
Taking into consideration the simulated spectra where we included some hybridization, it was found that a good match of the experimental data is obtained with 10% of Ce^{3+} at room temperature, which is slightly less that the 15% estimate done without the hybridization, and 30% at 600 °C

6.4. How to improve the research

It was seen how the $N_{4,5}$ edge can be used to follow the redox process, the spectra at high momentum transfer showed a visible change coherent with the calculated spectra, the changes were as expected; at low momentum transfer the changes in the spectra were partially justified, but the necessity of a finer simulation models has been highlighted.
Furthermore, since the sample were crafted from powders, no specific crystallography plane was favored. As explained in [6], the plane orientation may play a role in the

catalytic properties, it might be interesting to explore this dependence. Already some studies have been conducted on this topic, in [62] is reported the DFT + U characterization of ceria (111) and (110) surfaces and emerges that the the (110) plane present a sDOS with surface states and Ce ions with a dangling bond in the outwards direction with respect to the (110) plane. Moreover the calculations suggest that the oxygen vacancy prefer to thermalize on this plane instead on the (111), where they thermalize more in the subsurface [13, 21–23]. Nevertheless it is also reported that the (110) plane is less stable and increasing the temperature the surface tends to relax rearranging in (111) steps. The work conducted in [63] was studying the configuration and localization changes of the oxygen vacancy, with respect to the surface and the reduced Ce_{3+}, upon the application of some strain. This is useful as the possibility of tuning properties of ceria could be crucial for the technology applications.

Bibliography

[1] Changwei Xu and Pei Kang Shen. Electrochamical oxidation of ethanol on pt-ceo2/c catalysts. *Journal of Power Sources*, 142(1):27–29, 2005.

[2] Masatake Haruta, Tetsuhiko Kobayashi, Hiroshi Sano, and Nobumasa Yamada. Novel gold catalysts for the oxidation of carbon monoxide at a temperature far below 0 °c. *Chemistry Letters*, 16(2):405–408, 1987.

[3] M. Ozawa and C.-K. Loong. In situ x-ray and neutron powder diffraction studies of redox behavior in ceo2-containing oxide catalysts. *Catalysis Today*, 50(2):329–342, 1999.

[4] Friedrich Esch, Stefano Fabris, Ling Zhou, Tiziano Montini, Cristina Africh, Paolo Fornasiero, Giovanni Comelli, and Renzo Rosei. Electron localization determines defect formation on ceria substrates. *Science*, 309(5735):752–755, 2005.

[5] Yong Li, Shikun Li, Marcus Bäumer, Elena A. Ivanova-Shor, and Lyudmila V. Moskaleva. What changes on the inverse catalyst? insights from co oxidation on au-supported ceria nanoparticles using ab initio molecular dynamics. *ACS Catalysis*, 10(5):3164–3174, 2020.

[6] Kuan Chang, Haochen Zhang, Mu-jeng Cheng, and Qi Lu. Application of ceria in co2 conversion catalysis. *ACS Catalysis*, 10(1):613–631, 2020.

[7] Rashid Mehmood, Sajjad S. Mofarah, Wen-Fan Chen, Pramod Koshy, and Charles C. Sorrell. Surface, subsurface, and bulk oxygen vacancies quantified by decoupling and deconvolution of the defect structure of redox-active nanoceria. *Inorganic Chemistry*, 58(9):6016–6027, 2019.

[8] Kazuhiro Yamamoto, Takeshi Hashishin, Motohide Matsuda, Nan Qiu, Zhenquan Tan, and Satoshi Ohara. High-performance ni nanocomposite anode fabricated from gd-doped ceria nanocubes for low-temperature solid-oxide fuel cells. *Nano Energy*, 6:103–108, 2014.

[9] Chunwen Sun, Hong Li, and Liquan Chen. Nanostructured ceria-based materials: synthesis, properties, and applications. *Energy Environ. Sci.*, 5:8475–8505, 2012.

[10] Qi Fu, Howard Saltsburg, and Maria Flytzani-Stephanopoulos. Active nonmetallic au and pt species on ceria-based water-gas shift catalysts. *Science*, 301(5635):935–938, 2003.

[11] M. Melchionna and P. Fornasiero. The role of ceria-based nanostructured materials in energy applications. *Materials Today*, 17(7):349–357, 2014.

[12] Xin-Pu Fu, Li-Wen Guo, Wei-Wei Wang, Chao Ma, Chun-Jiang Jia, Ke Wu, Rui Si, Ling-Dong Sun, and Chun-Hua Yan. Direct identification of active surface species for the water–gas shift reaction on a gold–ceria catalyst. *Journal of the American Chemical Society*, 141(11):4613–4623, 2019. PMID: 30807152.

[13] Fei Wang, Min Wei, David G. Evans, and Xue Duan. Ceo2-based heterogeneous catalysts toward catalytic conversion of co2. *J. Mater. Chem. A*, 4:5773–5783, 2016.

[14] Alessandro Longo, Stavros Alexandros Theofanidis, Chiara Cavallari, Nadadur Veeraraghavan Srinath, Jiawei Hu, Hilde Poelman, Maarten K. Sabbe, Christoph J. Sahle, Guy B. Marin, and Vladimir V. Galvita. What makes fe-modified mgal2o4 an active catalyst support? insight from x-ray raman scattering. *ACS Catalysis*, 10(12):6613–6622, 2020.

[15] M. Verónica Ganduglia-Pirovano, Alexander Hofmann, and Joachim Sauer. Oxygen vacancies in transition metal and rare earth oxides: Current state of understanding and remaining challenges. *Surface Science Reports*, 62(6):219–270, 2007.

[16] Shuyan Song, Xiao Wang, and Hongjie Zhang. Ceo2-encapsulated noble metal nanocatalysts: enhanced activity and stability for catalytic application. *NPG Asia Materials*, 7(5):e179–e179, May 2015.

[17] Tiziano Montini, Michele Melchionna, Matteo Monai, and Paolo Fornasiero. Fundamentals and catalytic applications of ceo2-based materials. *Chemical Reviews*, 116(10):5987–6041, 2016. PMID: 27120134.

[18] Yang Zhang, Shuna Zhao, Jing Feng, Shuyan Song, Weidong Shi, Dan Wang, and Hongjie Zhang. Unraveling the physical chemistry and materials science of ceo2-based nanostructures. *Chem*, 7(8):2022–2059, 2021.

[19] David R. Mullins. The surface chemistry of cerium oxide. *Surface Science Reports*, 70(1):42–85, 2015.

[20] Bingyun Ao, Ruizhi Qiu, and Shu-Xian Hu. First-principles insights into the oxidation states and electronic structures of ceria-based binary, ternary, and quaternary oxides. *The Journal of Physical Chemistry C*, 123(1):175–184, 2019.

[21] G. E. Murgida, V. Ferrari, M. Verónica Ganduglia-Pirovano, and A. M. Llois. Ordering of oxygen vacancies and excess charge localization in bulk ceria: A DFT + u study. *Phys. Rev. B*, 90:115120, Sep 2014.

[22] M Verónica Ganduglia-Pirovano, Juarez LF Da Silva, and Joachim Sauer. Density-functional calculations of the structure of near-surface oxygen vacancies and electron localization on ceo2(111). *Physical Review Letters*, 102(2):026101, Jan 2009.

[23] Jan-Frederik Jerratsch, Xiang Shao, Niklas Nilius, Hans-Joachim Freund, and Cristina and Popa. Electron localization in defective ceria films: A study with scanning-tunneling microscopy and density-funct. *Phys. Rev. Lett.*, 106:246801, Jun 2011.

[24] Ken ichi Fukui, Yoshimichi Namai, and Yasuhiro Iwasawa. Imaging of surface oxygen atoms and their defect structures on ceo2(1 1 1) by noncontact atomic force microscopy. *Applied Surface Science*, 188:252–256, 2002.

[25] Yoshimichi Namai, Ken-Ichi Fukui, and Yasuhiro Iwasawa. Atom-resolved noncontact atomic force microscopic and scanning tunneling microscopic observations of the structure and dynamic behavior of ceo2(111) surfaces. *Catalysis Today*, 85(2):79–91, 2003. Metallic Oxides: Filling the Gap between Catalysis and Surface Science.

[26] Stefan Torbrügge, Michael Reichling, Atsushi Ishiyama, Seizo Morita, and Oscar Custance. Evidence of subsurface oxygen vacancy ordering on reduced ceo2(111). *Physical Review Letters*, 99(5):056101, Aug 2007.

[27] Alessandro Longo, Leonarda F. Liotta, Giuseppe Pantaleo, Francesco Giannici, Anna Maria Venezia, and Antonino Martorana. Structure of the metal–support interface and oxidation state of gold nanoparticles supported on ceria. *The Journal of Physical Chemistry C*, 116(4):2960–2966, 2012.

[28] Giulio Deganello, Francesco Giannici, Antonino Martorana, Giuseppe Pantaleo, Antonio Prestianni, Antonella Balerna, Leonarda F. Liotta, and Alessandro Longo. Metalsupport interaction and redox behavior of pt(1 wt %)/ce0.6zr0.4o2. *The Journal of Physical Chemistry B*, 110(17):8731–8739, 2006. PMID: 16640429.

[29] Alessandro Longo, Antonella Balerna, Francesco d'Acapito, Fabio D'Anca, Francesco Giannici, Leonarda F. Liotta, Giuseppe Pantaleo, and Antonino Martorana. A new

cell for the study of *in situ* chemical reactions using X-ray absorption spectroscopy. *Journal of Synchrotron Radiation*, 12(4):499–505, Jul 2005.

[30] Gianfranco Pacchioni. Electronic interactions and charge transfers of metal atoms and clusters on oxide surfaces. *Phys. Chem. Chem. Phys.*, 15:1737–1757, 2013.

[31] J. C. Frost. Junction effect interactions in methanol synthesis catalysts. *Nature*, 334(6183):577–580, Aug 1988.

[32] Rohit Sharma. X-ray raman scattering investigation on cerium oxide based systems. 2021.

[33] D. Widmann and R. J. Behm. Activation of molecular oxygen and the nature of the active oxygen species for co oxidation on oxide supported au catalysts. *Accounts of Chemical Research*, 47(3):740–749, 2014. PMID: 24555537.

[34] Marno Lohrenscheit and Christian Hess. Direct evidence for the participation of oxygen vacancies in the oxidation of carbon monoxide over ceria-supported gold catalysts by using operando raman spectroscopy. *ChemCatChem*, 8(3):523–526, 2016.

[35] Maria Pia Casaletto, Alessandro Longo, Anna Maria Venezia, Antonino Martorana, and Antonio Prestianni. Metal-support and preparation influence on the structural and electronic properties of gold catalysts. *Applied Catalysis A: General*, 302(2):309–316, 2006.

[36] Li-Wen Guo, Pei-Pei Du, Xin-Pu Fu, Chao Ma, Jie Zeng, Rui Si, Yu-Ying Huang, Chun-Jiang Jia, Ya-Wen Zhang, and Chun-Hua Yan. Contributions of distinct gold species to catalytic reactivity for carbon monoxide oxidation. *Nat Commun*, 7:13481, November 2016.

[37] Yang He, Jin-Cheng Liu, Langli Luo, Yang-Gang Wang, Junfa Zhu, Yingge Du, Jun Li, Scott X. Mao, and Chongmin Wang. Size-dependent dynamic structures of supported gold nanoparticles in co oxidation reaction condition. *Proceedings of the National Academy of Sciences*, 115(30):7700–7705, 2018.

[38] Alessandro Longo, Francesco Giannici, Maria Pia Casaletto, Mauro Rovezzi, Christoph J. Sahle, Pieter Glatzel, Yves Joly, and Antonino Martorana. Dynamic role of gold d-orbitals during co oxidation under aerobic conditions. *ACS Catalysis*, 12(6):3615–3627, 2022.

[39] Yanggang Wang, Donghai Mei, Vassiliki Alexandra Glezakou, Jun Li, and Roger J. Rousseau. Dynamic formation of single-atom catalytic active sites on ceria-supported gold nanoparticles. *Nature Communications*.

[40] O. V. Safonova, A. A. Guda, C. Paun, N. Smolentsev, P. M. Abdala, G. Smolentsev, M. Nachtegaal, J. Szlachetko, M. A. Soldatov, A. V. Soldatov, and J. A. van Bokhoven. Electronic and geometric structure of ce3+ forming under reducing conditions in shaped ceria nanoparticles promoted by platinum. *The Journal of Physical Chemistry C*, 118(4):1974–1982, 2014.

[41] Yves Joly, Chiara Cavallari, Sergey A. Guda, and Christoph J. Sahle. Full-potential simulation of x-ray raman scattering spectroscopy. *Journal of Chemical Theory and Computation*, 13(5):2172–2177, 2017. PMID: 28430428.

[42] Joachim Bansmann, Ali M. Abdel-Mageed, Shilong Chen, Corinna Fauth, Thomas Häring, Gabriela Kučerová, Yuchen Wang, and R. Jürgen Behm. Chemical and electronic changes of the ceo2 support during co oxidation on au/ceo2 catalysts: Time-resolved operando xas at the ce liii edge. *Catalysts*, 9(10), 2019.

[43] Ali M. Abdel-Mageed, Shilong Chen, Corinna Fauth, Thomas Häring, and Joachim Bansmann. Fundamental aspects of ceria supported au catalysts probed by in situ/-operando spectroscopy and tap reactor studies. *ChemPhysChem*, 22(13):1302–1315, 2021.

[44] Alayna Bone. Reducing taiwan's dependence on the chinese-dominated market for rare earth elements. *global Taiwan*, 7(15).

[45] Environmental geochemistry of cerium: Applicarion and toxicology of cerium oxyde nanoparticles. 2015.

[46] Kai Li, Ji Chen, and Dan Zou. Extraction and recovery of cerium from rare earth ore by solvent extraction. 2018.

[47] Yujian Zhou, Stephen Schulz, Jan Haberstroh, Marco Wenzel, Hao Du, and Jan J. Weigand. Ceres processseparation of cerium from lanthanum by redox extraction and stripping. *ACS Sustainable Chemistry & Engineering*, 10(49):16290–16298, 2022.

[48] Robert Hull, Jürgen Parisi, R. Osgood, Hans Warlimont, G. Liu, and Bernard Jacquier. *Spectroscopic Properties of Rare Earth in Optical Materials*, volume 83. 01 2005.

[49] K Hämäläinen and S Manninen. Resonant and non-resonant inelastic x-ray scattering. *Journal of Physics: Condensed Matter*, 13(34):7539, aug 2001.

[50] S. Huotari, Ch. J. Sahle, Ch. Henriquet, A. Al-Zein, K. Martel, L. Simonelli, R. Verbeni, H. Gonzalez, M.-C. Lagier, C. Ponchut, M. Moretti Sala, M. Krisch, and G. Monaco. A large-solid-angle X-ray Raman scattering spectrometer at ID20 of

the European Synchrotron Radiation Facility. *Journal of Synchrotron Radiation*, 24(2):521–530, Mar 2017.

[51] Marco Magnaterra. Crystal field scheme of the heavy fermion system cerh2as2 studied by means of x-ray absorption and x-ray raman scattering spectroscopy. 2019.

[52] G. Margaritondo. A Primer in Synchrotron Radiation: Everything You Wanted to Know about SEX (Synchrotron Emission of X-rays) but Were Afraid to Ask. *Journal of Synchrotron Radiation*, 2(3):148–154, May 1995.

[53] Ch. J. Sahle, A. Mirone, J. Niskanen, J. Inkinen, M. Krisch, and S. Huotari. Planning, performing and analyzing X-ray Raman scattering experiments. *Journal of Synchrotron Radiation*, 22(2):400–409, Mar 2015.

[54] Gabriel Vivó-Truyols and Peter J. Schoenmakers. Automatic selection of optimal savitzkygolay smoothing. *Analytical Chemistry*, 78(13):4598–4608, 2006. PMID: 16808471.

[55] Alessandro Mirone. Hilbert++ manual. 07 2007.

[56] Alessandro Mirone, Maurizio Sacchi, and Susana Gota. Ligand-field atomic-multiplet calculations for arbitrary symmetry. *Phys. Rev. B*, 61:13540–13544, May 2000.

[57] Alessandro Longo, Romain Wernert, Antonella Iadecola, Christoph J. Sahle, Lorenzo Stievano, Laurence Croguennec, Dany Carlier, and Alessandro Mirone. An original empirical method for simulating v l2,3 edges: The example of kvpo4f and kvopo4 cathode materials. *The Journal of Physical Chemistry C*, 126(46):19782–19791, 2022.

[58] R. A. Gordon, G. T. Seidler, T. T. Fister, M. W. Haverkort, G. A. Sawatzky, A. Tanaka, and T. K. Sham. High multipole transitions in nixs: Valence and hybridization in 4f systems. *Europhysics Letters*, 81(2):26004, dec 2007.

[59] Tomá š Duchoň, Marie Aulická, Eike F. Schwier, Hideaki Iwasawa, Chuanlin Zhao, Ye Xu, Kate řina Veltruská, Kenya Shimada, and Vladimír Matolín. Covalent versus localized nature of $4f$ electrons in ceria: Resonant angle-resolved photoemission spectroscopy and density functional theory. *Phys. Rev. B*, 95:165124, Apr 2017.

[60] Takeshi Matsukawa, Akinori Hoshikawa, and Toru Ishigaki. Temperature-induced structural transition of ceria by bulk reduction under hydrogen atmosphere. *CrystEngComm*, 20:4359–4363, 2018.

[61] Heike C Herper, Olga Yu Vekilova, Sergei I Simak, Igor Di Marco, and Olle Eriksson.

Localized versus itinerant character of 4f-states in cerium oxides. *J Phys Condens Matter*, 32(21):215502, May 2020.

[62] Stefano Fabris, Gianpaolo Vicario, Gabriele Balducci, Stefano de Gironcoli, and Stefano Baroni. Electronic and atomistic structures of clean and reduced ceria surfaces. *The Journal of Physical Chemistry B*, 109(48):22860–22867, 2005. PMID: 16853978.

[63] Zhong-Kang Han, Lei Zhang, Meilin Liu, Maria Verónica Ganduglia-Pirovano, and Yi Gao. The structure of oxygen vacancies in the near-surface of reduced ceo2 (111) under strain. *Frontiers in Chemistry*, 7, 2019.

List of Figures

1.1 Local structure of Ce ions in ceria 3
1.2 Spill over dynamics 5
1.3 NPs redox dynamics on ceria 7

2.1 Multiplet energy configuration 14
2.2 X-ray Raman inelastic scattering schematics 15
2.3 $4d^{10}4f^1$ to $4d^94f^2$ transition scheme 19

3.1 Synchrotron drawing 22
3.2 ID20 optic schematics 23
3.3 ID20 large-solid-angle x-ray Raman spectrometer 24
3.4 Ceria coated with Au NPs 25
3.5 Sample environment 26

4.1 ROIs selection 30
4.2 Compton removal for low $\boldsymbol{q}$ 31
4.3 Compton removal for high $\boldsymbol{q}$ 31
4.4 Sample experimental spectra 32
4.5 Reference experimental spectra 33

5.1 Hybridization effects on Ce^{4+} spectrum 38
5.2 Experimental and computed spectra 40
5.3 Low temperature experimental spectrum 41
5.4 High temperature experimental spectrum 42

A | Appendix A
code example

Here there are reported some of the codes used for the data analysis and the simulations with Hilbert++. Hilbert++ runs on linux and requires a conda-like environment. Any AI will show you how to install one on your computer in one or two lines of commands

A.1. h++

The simulations reported in this thesis were conducted using Hilbert++ 1.8 and 1.13, for the user point of view, it does not change that much. To run this you need to install the version of Hilbert++ that were provided to you, following the instructions in the README file in the installation folder.

```
home:~$ source ~/directory/to/miniconda3/bin/activate
(base) home:~$ conda activate h++1_13
(hpp1_13) home:~$
```

At this point we are ready to run the simulations we need. We can navigate to the folder where your code is saved in a general text file. In the next lines there will be reported the code we used to simulate both OS of Ce. The one that are not commented are the one that will be used, to switch we just need to switch the # sings.

```
transition = "4d4f"
atom = "Ce"

# Ce3+ #this needs to stay commented
#occupancy = 1
# Ce4+ #this needs to stay commented as well
occupancy = 0

bonds = [
```

```
10      [-1.352800,-1.352800,-1.352800],
11      [-1.352800,-1.352800,1.352800],
12      [-1.352800,1.352800,-1.352800],
13      [-1.352800,1.352800,1.352800],
14      [1.352800,-1.352800,-1.352800],
15      [1.352800,-1.352800,1.352800],
16      [1.352800,1.352800,-1.352800],
17      [1.352800,1.352800,1.352800]
18   ]
19
20  vc_d0 = 0.0
21  vc_d1 = 0.0
22  vc_f0 = 0.02
23  vc_f1 = 0.01
24  vc_g0 = 0.0
25  vc_g1 = 0.0
26
27  de = 0.001
28
29  q_exp = 9.5 #3.5
30
31  temperature = 0.025
32
33  grid_shape = [10,10]
34
35  # multipole_activation = [1,1,1,1]
36  multipole_activation = [1,1,1]
37
38  slater_reduction = 0.8
39
40  e_step_target = 0.05
41  #e_step_target = 0.1
```

Once we have chosen the parameters, we need to save it in a file `name_of_the_input_file.qdep`. This file will be used as parameter of the command `qdep_thomson_v{your_h++_version}`.

```
(hpp1_13) home:~$ qdep_thonmson_v1_13 name_of_the_input_file.qdep
```

The computation on a modern computer should take no more than a couple of minutes. The code will compute the spectrum relative to the transition defined in the input file, with a broadening of the peaks given by the `e_step_target` variable, chosing a small value, `0.005`, all the single transition lines will be observable. With higher values a pre-convolution will be performed. For details on this procedure I would recomend to contact the developer of the code. The spectrum will be saved in the `IXS.dat` file, in the directory from where we launched the code. Before launching other simulation with different parameters it is better to change this file's name, otherwise it will be overwritten by the new spectrum. How to use the rest of the variable has been explained in 5.1.
In the same section we have talked about hybridization. The full input file for the simulations that took into consideration the hybridization effects will be reported soon. We have to take into consideration that the parameter `relative_E_hopperA` has to change at each simulation run, between roughly 20 values for each momentum transfer. This is manageable by hand, but we wrote a simple bash script to automatize the process. In this particular script the version 1.18 of Hilbert++ has been used, but this does not change much in the script below.

```
1  #/usr/bin/bash
2  source /home/eugenio/miniconda3/bin/activate
3  conda activate h++1_8
4  for i in -5.0 -4.5 -4.0 -3.5 -3.0 -2.5 -2.0 -1.5 -1.0 -0.5
       0.0 0.5 1.0 1.5 2.0 2.5 3.0 3.5 4.0 4.5 5.0; do
5      for j in 3.0 9.5; do
6           fileinp=input_q_${j}_Ce4_4d4f_erel_$i
7           filename_tmp1=input_lowq_hyb_m2sopra14.qdep
8           filename_tmp2=input_lowq_hyb_m2sopra2.qdep
9           echo Nome: $fileinp, $fileinp.txt, $filename_tmp
10          echo -e "‘sed "s/qvalue/$j/g" $filename_tmp1‘ \n " >
                $fileinp.qdep
11          echo -e "‘sed "s/erel/$i/g" $filename_tmp2‘ \n " >>
               $fileinp.qdep
12          qdep_thomson_v1_8 $fileinp.qdep
13          new_dir=./Ce4+/q_${j}_erel_$i
14          mkdir $new_dir
15          mv $fileinp.qdep $new_dir
16          mv allspectra.h5 $new_dir
17          mv datas $new_dir
18          mv datas_baricenters $new_dir
```

```
19          mv datas_splitting $new_dir
20          mv debughopf $new_dir
21          mv f135_246.txt $new_dir
22          mv for_splot.txt $new_dir
23          mv IXS.dat $new_dir
24          mv versors_weights.h5 $new_dir
25          mv neutrality_convergence.txt $new_dir
26          mv qdep_thomson.log $new_dir
27      done
28  done
```

The `i` variable will define the `relative_E_hopperA` parameter, the `j` variable the momentum transfer. The `fileinp=input_q_$j_Ce3_4d4f_erel_$i` is the name of the file that will be used as the parameter of `qdep_thomson_v1_8` function. The `filename_tmp1` and `filename_tmp2` are the same script input file reported above for the simulation without hybridization, split in two for practical reasons of how the bash script function we chose work. The template input file are therefore:

```
1  transition = "4d4f"
2
3  atom = "Ce"
4  # Ce4+
5  occupancy=0
6  bonds = [
7      [-1.352800,-1.352800,-1.352800],
8      [-1.352800,-1.352800,1.352800],
9      [-1.352800,1.352800,-1.352800],
10     [-1.352800,1.352800,1.352800],
11     [1.352800,-1.352800,-1.352800],
12     [1.352800,-1.352800,1.352800],
13     [1.352800,1.352800,-1.352800],
14     [1.352800,1.352800,1.352800]
15  ]
16
17
18 vc_d0 = 0.0
19 vc_d1 = 0.0
20 vc_f0 = 0.02
```

```
21 vc_f1 = 0.01
22 vc_g0 = 0.0
23 vc_g1 = 0.0
24
25 de = 0.001
26
27 q_exp = qvalue
```

for `filename_tmp1`, and:

```
 1 temperature = 0.025
 2
 3 grid_shape = [10,10]
 4
 5 # multipole_activation = [1,1,1,1]
 6 multipole_activation = [1,1,1]
 7
 8 slater_reduction = 0.9
 9 e_step_target = 0.5
10
11 max_hoppedA = 1
12 relative_E_hopperA=erel
13 E_hopperA=44.16368662040769
14
15 vhopA_f0=0.5
16 vhopA_f1=0.1
17 stop_after_counters=False
18
19 F0=5.0
20 # e' sostituto inetgrale di slater F0 per la repulsione
      columbiana fra 4f 4f guscio parzialmente
21 #aperto o in genere guscio aperto
22
23 #DF0=5.0
24
25 #e' termine aggiuntivo che si aggiunge alla coulombiana fra 4
      d4f, che se no
26 # si prende uguqle a F0. Che aumenta la repulsione fra 4d e 4
```

```
   f che se no sarebbe la stessa.
27 #L effetto secondario e' quello di modificare nella
   configurazione eccitata
28 # ( quella di base va calibrata ) la natura dei legami
   leganti e antileganti (ampiezze
29 #che hanno sul cerio e ossigeno) perche' nello stato eccitato
    il termine F0 ( invece di
30 # F0+DF0 come quando l elettrone era su 4d)
31 #  agira'  sull'energia monoparticella di un 4f. Quindi un
   DF0 scompare ( rimangono 9 in 4d)
32 #  Questo produce un abbassamento di 4f che si traduce in una
    modificazione
33 # di quelli che sono gli orbitali leganti e antileganti negli
    autostati che si vedono
34 #  nello spettro
35
36 #procedure con hybridzzazione
37 #1) max_hoppedA deve essere 1
38 #2) run relative_E_hopperA=0.0 con  E_hopperA=-2.0+4.146776e
   +01 commentato
39 # e stop_after_counters=True
40
41 #) quindi troba il valore in neutrality convergevce
   sotitusci
42 #) e run commentando relative_E_hopperA=0.0. e
   stop_after_counters=False
43
44 #) se usi DF0 devi rifare la procedura.
45
46 average_is_spherical = False
```

for `filename_tmp2`. The bash script replaces at each simulation run the variables `qvaule` and `erel` with the values `j` and `i` in the range defined. Then it concatenates the two input file in a single one and runs the simulation. At the end of the simulation it creates a directory for the values of the parameters and moves all the file generated by code, including and most importantly the IXS.dat file with the spectrum.

The rest of the data analysis has been conducted with Python.

A.2. Python scripts

To reproduce the broadening effects due to the interaction with the continuum and the experimental set up we have convoluted the simulation spectra a Fano function of order q. Since Hilbert++ reproduces well the spectral features but the absolute energy of the edge is shifted, the following script performs both the broadening of the simulation spectra and a shift of the energies, using an experimental spectrum as reference.

```
1  from scipy import *
2  from scipy import interpolate
3  import os
4  from scipy.interpolate import interp1d
5  import numpy as np
6  import matplotlib.pyplot as plt
7  import time
8  plt.isinteractive()
9
10 def read(fname):
11     spec= np.loadtxt(fname,unpack=False)
12     return spec
13
14 def gau_baseline(x,yg,spec,plot=False):
15     xref=spec[:,0]
16     yref=spec[:,1]
17
18     if plot:
19         plt.figure(1)
20         plt.plot(x,yg,label="data broadened")
21         plt.plot(xref,yref,label="data")
22         plt.legend()
23         plt.show()
24 #         plt.close()
25     norm = np.trapz(yg,x=x)
26     yn = yg/norm
27     return x,yn
28
29
30 def gau_scale(x, yn, expdata, x0data, fscale, plot=False):
```

```
31      xdata = expdata[:,0]
32      ydata = expdata[:,1]
33      xn = x+x0data
34      yns =yn*fscale
35
36      if plot:
37          plt.figure(2)
38          plt.plot(xn,yns,label="data broadened")
39          plt.plot(xdata,ydata,label="EXP data")
40          plt.legend()
41          plt.show()
42      return xn,yns
43
44  """
45  def gauss(x,x0,fwhm):
46      # area-normalized gaussian
47      sigma = fwhm/(2*np.sqrt(2*np.log(2)));
48      y = np.exp(-(x-x0)**2/2/sigma**2)/sigma/np.sqrt(2*np.pi)
49      return y
50  """
51
52  def fano(x,x0,fwhm,q):
53      # area-normalized gaussian
54      deltax0=0
55      eps=(x-x0-deltax0)/fwhm
56      y1=(q+eps)**2
57      y2=(1+eps**2)
58      y=y1/y2
59      return y/y.sum()
60
61  def broaden_linear(spec,params=[0.8, 4., -0, 20, 10.5],
        npoints=1000):
62      """
63      broadens a spectrum with a Gaussian of width params[0]
            below
64      params[2] and width params[1] above params[3], width
            increases
```

```
65      linear in between.
66      returns two-column numpy array of length npoints with
           energy and the broadened spectrum
67      """
68      evals = spec[:,0] #energy values
69      sticks= spec[:,1] #intensities -> sticks
70      print('len sticks: ', len(sticks))
71      f_min = params[0] #
72      f_max = params[1] #
73      e_min = params[2]
74      e_max = params[3]
75      q = params[4]
76      #print ("fano params", q)
77      e2    = np.linspace(np.min(evals)-10.0,np.max(evals)
           +10.0,npoints)
78      s2    = np.zeros(len(e2))
79      fwhm  = np.zeros(len(evals))
80      # FWHM: Constant  -- Linear -- Constant
81      #so what we are doing below is to set the FWHM costant to
            the the value f_min below e_min
82      #and set it to f_max above e_max. in between it changes
           linearly between f_min and f_max
83      A     = (f_max-f_min)/(e_max-e_min)
84      B     = f_min - A*e_min
85      fwhm = A*evals + B
86      fwhm[evals <= e_min] = f_min
87      fwhm[evals >= e_max] = f_max
88      for n in range(len(sticks)):
89         #s2 = s2 + sticks[n]*gauss(e2,evals[n],fwhm[n])
90          s2 = s2 + sticks[n]*fano(e2, evals[n], fwhm[n], q)
91          #if n % 50 == 0:
92          #    plt.plot(e2, s2/np.trapz(s2),label=np.trapz(s2))
93      spectrum = np.zeros((len(e2),2))
94      spectrum[:,0] = e2
95      spectrum[:,1] = s2
96      #plt.legend()
97      #plt.show()
```

```
98      return spectrum
99
100 def gau_save(fname, fname1, x0, gamma, q, x0data, fscale,
       params):
101     spec=read(fname)
102     print ("fano params start", x0, gamma, q)
103 #     spectrum=broaden_linear(spec,params=[0.6, 65.5, 16.5,
       20.5, 30.5],npoints=1000)
104 #   per cambiare l cnvoluzione modificare parametri: li passa
       poi alle broaden_linear
105 #     spectrum=broaden_linear(spec,params=[0.2, 10, 114, 140,
       130],npoints=1000) #high
106     spectrum=broaden_linear(spec,params = params,npoints
          =1000)#3.7, 120, 140, 5],npoints=1000) #low
107     x=spectrum[:,0]
108     yconv=spectrum[:,1]
109     """
110     confronto conv e dato ottenuto da hilbert++
111     """
112     x,yn = gau_baseline(x,yconv, spec, plot=False)
113     ret = np.asarray( (x,yn) )
114     """
115     confronto conv scalata  x e y e data sperimenatale
116     """
117     expdata=read(fname1)
118     xn,yns = gau_scale(x, yn, expdata, x0data, fscale, plot=
          True)
119     print("params for expdata:", x0data, fscale)
120     retf = np.asarray ( (xn,yns))
121     np.savetxt('broad.ris',retf.T,fmt="%10.5e")
122
123
124 def gau_test():
125
126
127     erel=erelative
```

```
128     pathc = "/home/eugenio/hilberto/hybridation/test/Ce4+/q_3
           .0_erel_2.0_etar_0.05"
129     pathe = "/home/eugenio/data/ih-ch-1634/raw_data/regressed
           /"
130     gau_save(os.path.join(pathc,"IXS.dat"),pathe+"117
           _CeO2_aldrich_fresh_sum_lowq_regressed_smoothed.dat",
131             x0=1, gamma=0.5, q=1.5, x0data=-1.5, fscale=1.25
                   e0, params = [0.8, 6.0, 120, 140, erel]) #low
                   [0.8, 6.0, 120, 140, 5] #high[0.2, 10, 114,
                   140, 130]
132     print("erel: ", erel)
133
134 def gau():
135     sum_data('','')
136
137 if __name__ == "__main__":
138     gau_test()
```

Here `erel` is used as variable to test different q values for the Fano function order. To test more q values the following bash script has been used:

```
1 #!/usr/bin/bash
2
3 for i in  2.3 2.32; do #2.675 2.7
4     echo -e "`sed "s/erelative/$i/g" fila_pyxfano_template.py
          ` \n " > fila_pyxfano_fano.py
5     echo "erel: $i"
6     python3 fila_pyxfano_fano.py
7     done
```

but by changing the variable `erel` in the Python code above to other parameters of the convolution we can test different values and chose the one that fits the best.

B | Appendix B
Synchrotron beam properties

Synchrotrons facilities are big circular rings made by straight parts, Insertion Devices or ID, and curved ones, Bending Magnets or BM. In the ring electrons are accelerated to produce electromagnetic radiation. The electrons become, inside synchrotrons, moving sources and are characterized by high angular collimation, and high power. The electrons that moves inside the synchrotron ring have relativistic speeds. So Lorentz transformations have a role in the understanding properties of synchrotron radiation.

B.1. Relativistic effects

The Doppler effect induces a significant change in the central emission frequency of the photon emitted in the laboratory frame of reference with respect to the electrons frame of reference. The easiest way to derive the shift is to consider the following relations; the subscription L stands for the the laboratory and S for the source, the electron in our case:

$$\beta = v/c, \tag{B.1a}$$

$$\gamma = \frac{1}{\sqrt{1-\beta^2}}, \tag{B.1b}$$

$$x_L = \gamma(x_S + vt_S), \tag{B.2a}$$

$$y_L = y_S, \tag{B.2b}$$

$$t_L = \gamma(t_S + vx_S/c^2), \tag{B.2c}$$

The frame of reference is taken as the plane where the electrons move with their circular trajectory, with the x taken in the same instantaneous direction of the motion and y perpendicular to x. Now the shift is obtainable considering the energy and the momentum transformation in the two frames of reference:

$$p_{Lx} = \gamma(p_{Sx} + vE_S/c^2), \tag{B.3a}$$

$$p_{Ly} = p_{Sy}, \tag{B.3b}$$

$$E_L = \gamma(E_S + vp_{Sx}), \tag{B.3c}$$

and since the energy and the momentum of a photon are given by:

$$E = \hbar\omega, \tag{B.4}$$

$$p = \hbar\omega/c, \tag{B.5}$$

in our specific case of a photon directed as x we have:

$$E_S = \hbar\omega_S, \tag{B.6a}$$

$$p_{Sx} = \hbar\omega_S/c,\ p_{Sy} = 0, \tag{B.6b}$$

$$E_L = \hbar\omega_L, \tag{B.6c}$$

$$p_{Lx} = \hbar\omega_L/c,\ p_{Ly} = 0, \tag{B.6d}$$

we can substitute in (B.3c) equation (B.6a) and obtain immediately:

$$\omega_L = \omega_S\sqrt{\frac{1+\beta}{1-\beta}} = \omega_S\gamma(1+\beta) \tag{B.7}$$

that when $v \to c$, then $\beta \to 1$, $\gamma(1+\beta) \approx 2\gamma$ and then:

$$\omega_L = \omega_S\gamma(1+\beta) \approx 2\gamma\omega_S, \tag{B.8}$$

if we look on the x axis.
If we want to look in a direction shifted of an angle θ_L with respect to x then we would obtain:

$$\omega_L = \frac{\omega_S}{\gamma(1-\beta cos\theta_L)}. \tag{B.9}$$

The matter of the angle θ_L is also an interesting one. Understanding how the angles of emission of the radiation change between the electron frame of reference and the laboratory one, give unique insight on the reason of the the extraordinarily high collimation of the synchrotron beam.
If we were to consider a non-relativistic moving source of sound wave moving with velocity

v, an arbitrary angle of emission θ_S would be defined as

$$tan\theta_S = u_{Sy}/u_{Sx}, \tag{B.10}$$

with u_{Si} the components of the wave velocity vector $\mathbf{u}_S$ in the direction of the emission. From the detector PoV, the same components undergo classical transformation and became $u_{Ly} = u_{Sy}$ and $u_{Lx} = u_{Sx} + v$ and the angle θ_L can be expressed as:

$$tan\theta_L = \frac{u_S sin\theta_S}{u_S cos\theta_S + v} = \frac{sin\theta_S}{cos\theta_S + v/u_S}. \tag{B.11}$$

Same applies for the photons emitted by an electron moving in a synchrotron: the pattern of emission for an electron with a centripetal acceleration is proportional to

$$\alpha(1 - sin^2\theta cos^2\phi) \tag{B.12}$$

where θ and ϕ are the angles that the photons emission direction forms respectively with the velocity of the electrons and with the plane of the ring.
The angles θ_L and θ_S can be defined with the momenta x and y components in the two frames of reference, we can use (B.3a), (B.3b) and (B.5)[1] to obtain the relation between the two angles in the relativistic source case:

$$\begin{aligned} tan\theta_L = p_{Ly}/p_{Lx} = \\ = \frac{p_{Sy}}{\gamma(p_{Sx} + vE_S/c^2)} = \\ = \frac{(\hbar\omega_S/c)sin\theta_S}{\gamma((\hbar\omega_S/c)cos\theta_S + v\hbar\omega_S/c^2)} \end{aligned} \tag{B.13}$$

that remembering (B.1a)[2] simplifies to

$$tan\theta_L = \frac{sin\theta_S}{\gamma(cos\theta_S + \beta)} \approx \frac{sin\theta_S}{\gamma(cos\theta_S + 1)} \tag{B.14}$$

since $\beta \approx 1$.
In the plane of the ring, there are no photons emitted in the direction perpendicular to the speed of the electrons. Which is what (B.12) tells us when $\theta_S = \pi/2$ and $\phi = 0$. Which means means that in the frame of reference of the laboratory, all the emitted photons will

[1] $p_{Lx} = \gamma(p_{Sx} + vE_S/c^2)$ (B.3a), $p_{Ly} = p_{Sy}$ (B.3b), $p = \hbar\omega/c$, (B.5).
[2] $\beta = v/c$ (B.1a)

be inside a cone with angular width of:

$$\theta_L = \frac{sin\,\pi/2}{\gamma(cos\,\pi/2+1)} = \frac{1}{\gamma}, \tag{B.15}$$

that for relativistic particle is incredibly small.

B.2. Undulators

Undulators insertion devices consists in a periodic repetition of magnets of opposite dipole that cause the electrons to wiggle and emit very sharp peaks of radiation with a specific frequency. For a classical electron the frequency would be give by the speed of the electron divided by the length of a period. The electrons in a synchrotron are moving at relativistic speed, so we have to consider that they'll experience a period of oscillation shorter than what it is in the laboratory frame. For the electron the period of the undulator λ_L has to be corrected by a factor $1/\gamma$. This leads to an emitted photon on the x axis with energy $E_S = 2\pi c\gamma/\lambda_L$, that, as we have seen in the previous section with (B.8), becomes:

$$E_L = 4\pi\gamma^2 c/\lambda_L \tag{B.16}$$

in the frame of the laboratory.
If we were to look at photons coming with an angle θ_L with respect to x then we the energy is expressed by:

$$E_L = 4\pi\gamma^2 c/\lambda_L \left(\frac{1}{1+\theta_L^2\gamma^2}\right). \tag{B.17}$$

Furthermore, we have to consider that the undulation induced to the electrons decrease their velocity in the x direction and the energy has to be corrected by an approximated factor of $1/(1+\frac{1}{2}\mathbf{K}^2)$, with $\mathbf{K} = e\mathbf{B}_L\lambda_L/2\pi c m_0$ [3], giving a final expression of:

$$E_L \approx (4\pi\hbar c\gamma^2/\lambda_L)\left(\frac{1}{1+\frac{1}{2}\mathbf{K}^2+\theta_L^2\gamma^2}\right) \tag{B.18}$$

called first-harmonic undulator equation.
Each module of the undulator acts as a single grate in diffraction gratings. The bandwidth of an undulator with N_u periods is therefore given by the general result of:

$$\Delta\hbar\omega_L/\hbar\omega_L = 1/N_u. \tag{B.19}$$

[3] $\mathbf{B}_L$ is the magnetic field, m_0 is the rest mass of the electron

We can't lower the bandwidth arbitrarily low increasing the number of periods because the bandwidth is also determined by the energy spread of the electrons in the electron beam in the ring.

Acknowledgements

I want to thanks in particular Alessandro Longo and Christoph J. Sahle for having guided me throughout my experience at ESRF and well beyond, teaching me stuff, showing me other and suggesting the rest, and also for reviewing my thesis; Prof. Marco Moretti for the same, all giving me the opportunity to conduct my thesis at the ESRF. Thanks to Emmanuelle de Clermont Gallerande for having conducted the experiments with us (with us mainly in her way), to Blanka Detlefs, Florent Gerbon, and Quentin Faure for the support they gave me at ID20, to Alessandro Mirone for taking the time to explain me his code and providing the templates to use it.

Thanks to all the people who contributed to making my life bearable in Milan for the last seven years, and to the ones that made my life bearable everywhere else. Thanks to my parents and to my sister for giving me infinite support. Thanks to all other siblings who don't register but in my heart[4]. Special mention to my sister Mery that she is suppose to graduate with me, and made the experience in Grenoble one of the best period in my life. Also to Mala and Giorgio that didn't let the rest of our friends pressure them and waited to graduated together, thanks boys. Unlike Lucy and Nik, that, quite egoistically, graduated already, but they did help make my life enjoyable in Milan and Grenoble as well. Thanks to Luca for roommating. Thanks to Alberto, Lia and Anita, just because.

[4] aaaww, I know right?